Inferring the Spatial and Energy Distribution of Gamma Ray Burst Sources. III. Anisotropic Models

Thomas J. Loredo and Ira M. Wasserman

Center for Radiophysics and Space Research, Cornell University, Ithaca, NY 14853-6801

ABSTRACT

We use Bayesian methods to study anisotropic models for the distribution of gamma ray burst intensities and directions reported in the *Third BATSE Catalog* (3B catalog) of gamma ray bursts. We analyze data obtained using both the 64 ms and 1024 ms measuring timescales. We study both purely local models in which burst sources ("bursters") are presumed to be distributed in extended halos about the Galaxy and M31, and mixed models consisting of a cosmological population of standard candle bursters and a local population distributed throughout a standard Bahcall-Soneira dark matter halo with a 2 kpc core. A companion paper studies isotropic models, including a variety of cosmological models, using the same methodology adopted here, allowing us to rigorously and quantitatively compare isotropic and anisotropic models. We find that the purely local models we have studied can account for the 3B data as successfully as cosmological models, provided one considers halos with core sizes significantly larger than those used to model the distribution of dark matter. A preference for cosmological over local models, or vice versa, must therefore be justified using information other than the distribution of burst directions and intensities. We infer core sizes for the halo distribution that are smaller than one might expectbased on popular semiquantitative arguments that consider the superposed dipole moments of shells centered on the Galactic center, and show why such arguments can lead to unwarranted conclusions. We also find that the 3B data do not constrain the width of power-law luminosity functions for burst sources. This disagrees with the findings of previous studies; we elucidate the qualitative reasons for the lack of a constraint, and discuss why our results differ from those of earlier studies. Our analysis of mixed models finds two families of models that can successfully account for the data: models with up to 20% of observed bursts in a bright local population visible to $\sim$ 50 kpc; and models with up to 50% of observed bursts in a dim local population visible only nearby (to less than a disk scale height). These models fit as well or better than purely cosmological models. They indicate that a surprisingly large local, anisotropic component could be present whose size is comparable to the sizes of hypothetical classes of bursts inferred from analyses of temporal and spectral characteristics. Finally, as in our study of isotropic models, we find substantial systematic differences between

results based on 64 ms and 1024 ms data, indicating that a thorough understanding of the distribution of burst intensities and directions is likely to require detailed analysis of temporal properties.

Subject headings: Gamma rays: bursts

1. Introduction

At the time of the launch of the *Compton Gamma Ray Observatory* (*CGRO*), the prevailing viewpoint among gamma ray astrophysicists was that gamma ray bursts originate in the vicinity of neutron stars distributed throughout the Galactic disk (see, e.g., the reviews of Liang and Petrosian 1985, and Higdon and Lingenfelter 1990). Perhaps the strongest evidence supporting this hypothesis was the detection of absorption-like features at energies of $\sim$ 10–50 keV in the spectra of bursts. The KONUS experiment provided the earliest evidence for the presence of such features (Mazets et al. 1981, 1982), but the most conclusive evidence came from instruments on the *Ginga* spacecraft (Murakami et al. 1988; Fenimore et al. 1988). The features observed by *Ginga* have high statistical significance, and can be well-modelled as being due to cyclotron scattering in a strongly magnetized plasma with field strength $B \sim 10^{12}$ G (Wang et al. 1989; Lamb et al. 1989). This field strength is typical of that associated with both rotation-driven and accretion-driven pulsars, suggesting that bursts are associated with strongly magnetized neutron stars. Further, requiring that a gravitationally confined scattering region be static implied that the burst sources so far observed were no further than a few hundred parsecs distant, otherwise the sources would have to be so luminous that radiation presure would drive the scattering plasma away from the source (Lamb, Wang, and Wasserman 1990; magnetic confinement may relax this constraint).

The hypothesis that bursters formed a disk population seemed consistent with the most direct information available about the spatial distribution of bursters: the distribution of burst directions and intensities. The apparent isotropy of the distribution of directions to bursts (Atteia et al. 1987; Golenetskii 1988; Hartmann and Epstein 1989; Hartmann and Blumenthal 1989) implied that we could be observing members of a disk population only to distances smaller than a disk scale height—the distance scale implied by magnetized neutron star models with a static cyclotron scattering region. Reconciling a disk population with the cumulative distribution of burst intensities (the "size-frequency" distribution) was somewhat more problematic. The cumulative distribution of burst fluences, S, or peak energy fluxes, F, was significantly flatter than the $-3/2$ power law expected from sampling a spatial distribution from well within its characteristic length scale, but it appeared that selection biases could account for much of the flattening (Yamagami and Nishimura 1986; Higdon and Lingenfelter 1986; Mazets and Golenetskii 1987; Paczynski and Long 1988; Schmidt, Higdon, and Hueter 1988). The burst peak count rate, C, was proposed as a less "biased" intensity measure than fluence or peak energy flux, and

the distribution of peak count rates appeared to be consistent with a $-3/2$ power law. Dispute remained over whether the distribution began to flatten for the dimmest bursts (Jennings 1988), but the number of faint bursts was too small to ascertain whether such bursts were anisotropically distributed, as one would expect if the faint bursts were observed from beyond a disk scale height. Hartmann, Epstein, and Woosley (1990) modelled the distribution of neutron stars in the Galaxy, and found the direction and intensity observations to be consistent with an association of bursts with Population I neutron stars, provided the distribution was sampled to distances beyond ~ 150 pc, but no greater than ~ 2 kpc.

Although the Galactic neutron star scenario appeared consistent with the observations, some investigators argued in favor of a cosmological origin for bursts (e.g., Usov and Chibisov 1975; van den Bergh 1983; Paczynski 1986; Goodman 1986). The combination of isotropy of burst directions and inhomogeneity implied by burst intensities is a natural characteristic of such models, provided the observations sample sources well beyond the local supercluster (Hartmann and Blumenthal 1989). An additional motivation for considering cosmological models was provided by Paczynski (1990) who, using a different model for the distribution of old neutron stars than that adopted by Hartmann, Epstein, and Woosley (1990), found a neutron star origin inconsistent with the distribution of burst directions and intensities. Together, the work of Paczynski and of Hartmann, Epstein, and Woosley implied that the consistency of the Galactic disk model with the observations depended on uncertain details of the models, particularly in regard to the distribution of birth velocities of pulsars and the detailed form of the Galactic potential (Hartmann, Epstein, and Woosley 1990).

Six years prior to the launch of *CGRO*, Meegan, Fishman, and Wilson (1985) reported detection of a single burst by a sensitive balloon-borne detector that should have seen ~ 43 bursts if the population of burst sources was spatially uniform to the distance sampled by the detector, conclusively demonstrating that the cumulative distribution of intensities of dim bursts was flatter than the homogeneous $-3/2$ power law. This was thought to be consistent with the Galactic disk paradigm, provided that the detector was able to see bursts from sources more distant than a disk scale height, hence detecting inhomogeneity in the source distribution. It was thus predicted that the Burst and Transient Source Experiment (BATSE) on board *CGRO* would find faint bursts concentrated in the Galactic plane, finally providing compelling evidence for the Galactic disk neutron star paradigm.

Within a year of the launch of CGRO, BATSE observations spectacularly refuted the Galactic disk neutron star hypothesis (Meegan, et al. 1992). The observations confirmed the inhomogeneity discovered with the earlier balloon observations: the cumulative distribution of the peak fluxes of BATSE bursts roughly follows a -1 power law and definitively rejects the $-3/2$ power law expected for a homogeneous distribution. Yet the distribution of the directions to these bursts is consistent with isotropy, with no significant concentration of burst sources in the Galactic plane. These basic features—apparent isotropy, and inhomogeneity—have been only more conclusively demonstrated by subsequent BATSE observations (Fishman et al. 1992, 1996).

Although the BATSE observations definitively rule out a Galactic disk origin for bursts, there is considerable controversy over whether the BATSE data favor cosmological models over local models that distribute burst sources in a large Galactic halo or corona, rather than in a disk population. Large scale isotropy and inhomogeneity are natural qualitative features of cosmological models for burst sources, so the BATSE observations have revitalized interest in such models. One can construct halo or coronal models that are consistent with the data, but they have length scales considerably larger than those for matter distributions known to be associated with the Galaxy prior to the BATSE observations, further fueling interest in cosmological models. But in the last five years, evidence has accumulated indicating that there may be a population of high velocity neutron stars with unbound or marginally bound orbits, very possibly forming a large Galactic corona (Lyne and Lorimer 1994; Frail 1996). Ironically, some of this evidence has been provided by observations of Soft Gamma Repeaters (SGRs; see, e.g., Rothschild 1996), another class of gamma ray transient studied with BATSE. This, combined with suggestive but so far unconclusive evidence for burst repetition (which is difficult to reconcile with most cosmological models) has revived interest in Galactic models, and enlivened the controversy over whether the data can discern between cosmological and local alternatives (see, for example, Lamb 1995 and Paczyński 1995).

This paper is the third in a series in which we apply the principles of Bayesian inference to the problem of inferring the spatial and energy distribution of burst sources from burst direction and intensity data provided by BATSE. In Paper I (Loredo and Wasserman 1995) we described the methodology and compared it to other methods in use. In Paper II (Loredo and Wasserman 1996), a companion paper to this one, we apply the method to isotropic models (including cosmological models), using the data from the recently released *Third BATSE Catalog* (Fishman et al. 1996; hereafter the 3B catalog). In the present paper, we use the method to study anisotropic models. Our method is uniquely suited to the study of these models, because it is the only method presently available that is capable of analyzing the distribution of burst directions and intensities *jointly*. Since all anisotropic physical models so far proposed have an anisotropy whose characteristics vary with burst intensity, only a method capable of analyzing the joint distribution can fully evaluate these models. In addition, since we are using the same method to study both isotropic and anisotropic models, we are able to quantitatively compare them. The Bayesian tool for doing this—the odds ratio—includes a factor that accounts for the size of the parameter spaces of models, resulting in an "Ockham's Razor" that automatically and objectively accounts for model complexity and parameter uncertainty in such comparisons.

We presume the reader to be familiar with the notation and methodology described in Papers I and II; §§ 2 and 3 of Paper II summarize this information. The next section presents an analysis of halo models whose burst rate density is spherically symmetric about the Galactic center and falls off with radius r like $1/[1 + (r/r_c)^2]$, where r_c is a core radius parameter; we analyze models with and without a similar halo centered on M31. We study models with "standard candle" and power law luminosity functions. In § 3, we analyze models that superpose two populations: a standard

candle halo population like those analyzed in § 2, and a standard candle cosmological population. For these models, we set the core size of the halo population equal to 2 kpc, the value inferred by Bahcall and Soneira (1980) in their study of the Galactic rotation curve. This allows us to obtain precise, model-dependent constraints on the fraction of bursts that could be associated with a known local matter distribution. We find this fraction can be quite high, even though the halo population has a relatively small core size. Finally, in § 4 we discuss some of the implications of the work reported here and in Paper II.

Before moving on to the results of our study, we note some additional distinguishing features of this study. No study has yet been published that has analyzed anisotropic models using the 3B data. This most recent BATSE catalog contains data for about twice as many bursts as the earlier 2B catalog (Fishman et al. 1994), so new analyses using this data are of obvious importance. In addition, we analyze data for two of the three trigger timescales included in the catalog: 64 ms (the shortest) and 1024 ms (the longest). Previous studies used only one timescale; most studies used the 1024 ms timescale. As shown in Paper II, the shapes of distributions of 64 ms and 1024 ms peak fluxes differ, and there is evidence that the additional structure present in the 1024 ms data is due to peak dilution (incorrect peak flux estimation when the peak duration is shorter than the measurement timescale). Thus it is important to analyze data from different timescales to ascertain what features of one's inferences are robust. Our method can be generalized to include temporal information about bursts, as outlined in Paper I; but the required information is absent from the 3B catalog, and such an analysis is beyond the scope of the current investigation.

Finally, we are not aware of a single study that calculated correct constraints for the unknown parameters of Galactic models, even using earlier BATSE data. Rather than using standard tools for calculating confidence regions, investigators instead computed goodness-of-fit statistics on grids throughout parameter space, and used contours of constant significance to constrain parameters (see, e.g., Hakkila et al. 1994). This is not a correct parameter estimation technique, and the resulting "significance regions" are of no use beyond determining whether the best-fit model is acceptable. Since similar techniques have been used in other fields, we devote Appendix A to a general discussion of the problems with this approach. In particular, we apply it to a simple Gaussian estimation problem, and show that the methodology adopted by earlier investigators leads to grossly incorrect confidence regions, and that the error *grows* with the size of the data set. By contrast, the Bayesian methodology produces probability densities for parameters of Galactic models for the 3B data, from which rigorous constraints on model parameters may be derived directly.

2. Overview of Method

As described in Paper I and summarized in § 2 of Paper II, Bayesian inference requires that a model fully specify the *differential burst rate*, $dR/d\Phi d\mathbf{n}$—the burst rate per unit time, peak flux, and steradian—as a function of peak flux Φ and direction $\mathbf{n}$. For most physical models,

including the halo models we analyze here, we calculate the differential burst rate from the *burst rate density*, $\dot{n}(\mathbf{r}, \Lambda; \mathcal{P})$, which gives the burst rate per unit time, volume, and peak luminosity for bursts from position $\mathbf{r}$ with peak luminosity Λ. Most such models have unknown parameters, here denoted collectively by $\mathcal{P}$. Once we have specified the burst rate density, we can straightforwardly calculate the differential burst rate according to equation (2.1) in Paper II. Here and throughout our papers, the term "peak luminosity" and the symbol Λ refer to the peak photon *number* luminosity, not the more common energy luminosity, L. Similarly, "peak flux" refers to the peak photon number flux, not to the energy flux, F. For convenience, we use these symbols to refer to the luminosity or flux in the nominal detected energy range of 50 to 300 keV.

We undertake two distinct and complementary statistical tasks: estimating or constraining unknown parameters in a particular burst rate density model; and comparing rival burst rate density models. Different calculations are required to address these tasks. Most previous analyses of the BATSE data did not distinguish these tasks; we discuss some consequences of this in Appendix A. The principal quantity underlying the Bayesian approach to these tasks is the likelihood function for the parameters $\mathcal{P}$ of a model, $\mathcal{L}(\mathcal{P})$. This is just the probability for obtaining the 3B data, presuming a particular model is true, with its parameters equal to $\mathcal{P}$. We discuss how to calculate $\mathcal{L}(\mathcal{P})$ in detail in Paper I; we offer a summary of the necessary calculations in § 2 of Paper II.

Once the likelihood is available, parameter estimation proceeds by examining the posterior distribution for the parameters: the normalized product of $\mathcal{L}(\mathcal{P})$ and a prior distribution for $\mathcal{P}$. We quote the mode of the posterior as the "best-fit" parameter point, and we present contours of constant probably density bounding regions containing a specified amount of integrated probability ("credible regions") as summaries of the constraints the data impose on the parameter values. We adopt the same conventions for prior probabilities and plots of posterior densities as described in § 2 of Paper II; that is, we choose parameter axes (linear or logarithmic) so that the prior density is constant, resulting in posterior densities that are simply proportional to the likelihood as a function of plotted parameters.

Model comparison proceeds by comparing the average likelihoods of competing models (using the prior as the averaging weight over the parameter space). The ratio of the average likelihood of one model to that of another is the *Bayes factor*, B; it is the odds in favor of the former model over the latter (presuming they would be given even odds in the absence of the data). Where possible, we also provide the results of an asymptotic frequentist maximum likelihood ratio test. Such a test is possible only for nested models; in contrast, the Bayes factor is appropriate for comparing any models. In addition, the averaging underlying the Bayes factor accounts for the sizes of the parameter spaces of the competing models, implementing a quantitative and objective "Ockham's Razor" that tends to favor simpler models over more complicated competitors.

Most burst rate density models can be written in the form

$$\dot{n}(\mathbf{r}, \Lambda; \mathcal{P}) = Af(\mathbf{r}, \Lambda; \mathcal{S}),$$

where A is an amplitude parameter and the remaining parameters, $\mathcal{S}$, are shape parameters. As we noted in Paper I, this separation is useful both because the shape and amplitude parameters typically reflect different physics, and because the amplitude parameter can be removed from the analysis *analytically* when we want to focus attention on the shape parameters alone. To make inferences about the shape parameters alone (taking into account the uncertainty in the amplitude parameter), we calculate the shape parameter likelihood function according to equation (2.9) in Paper II. To make inferences about all parameters, we calculate the full likelihood function according to equation (2.7) of Paper II.

Before proceeding to the results, we remind the reader that in § 3 of Paper II we note several approximations we must make in order to calculate the likelihood for the 3B data (these approximations must be made in *any* rigorous analysis, not just a Bayesian analysis). Some of those approximations have no effect on analyses of the isotropic models that are the focus of Paper II; these deserve spectial mention in this work. In particular, we note in Paper II that the systematic errors in the directions reported in the 3B catalog are not well understood (Graziani and Lamb 1996). The calculations reported here all use the reported systematic error (a constant error of 1.6°, to be added in quadrature with the statistical error). To test the robustness of our findings with respect to the size of the systematic errors, we have repeated several calculations with the systematic error increased to the value reported in the 2B catalog (4°). The resulting changes in the locations of credible regions are completely negligible. This is presumably because uncertainties on these small angular scales are not of great importance for constraining large angular scale anisotropy. The precise size and geometry of the direction uncertainties is more important for assessing models with structure on small angular scales, such as models that allow burst sources to repeat (see, e.g., Luo, Loredo, and Wasserman 1996). More troubling is the fact the new direction algorithm used to produce the 3B catalog significantly changed the inferred directions of many of the bursts included in the 2B catalog; but the peak flux estimates of these bursts have not been recalculated using the new directions. We have no way of estimating the resulting systematic uncertainty in the peak flux estimates, although we note in Paper II some reasons to expect them to be small.

3. Halo Models

3.1. Standard Candle Models

We begin by considering "standard candle" halo models, for which we can write the burst rate density as

$$\dot{n}(\mathbf{r}, \Lambda) = \dot{n}(\mathbf{r})\, \delta(\Lambda - \Lambda_h), \tag{1}$$

where Λ_h is the standard candle peak photon number luminosity. We take the spatial dependence of the burst rate density to be spherically symmetric around the center of the host galaxy (the

Milky Way or M31), falling with galactocentric radius, r, according to

$$\dot{n}(\mathbf{r}) = \frac{\dot{n}_0}{1 + \left(\frac{r}{r_c}\right)^2}, \tag{2}$$

where r_c is the core radius, and $\dot{n}_0$ is the burst rate per unit volume at $r = 0$. The rate density is thus roughly constant for $r \lesssim r_c$, and falls like r^{-2} beyond r_c. This is the form often used to model the distribution of dark matter; in these applications, estimated core sizes are typically a few kiloparsecs (Bahcall and Soneira 1980). Some investigators refer to halos with core sizes significantly larger than those of dark matter halos as "coronas." This spherically symmetric model, though widely used, is clearly unrealistic for distances of order or larger than ~ 300 kpc (about half the distance to M31). This is because the dynamical timescales at these distances are of order the Hubble time. We expect the distribution of matter at these distances to reflect initial conditions, and thus do not consider it plausible that it exhibit the isotropy or radial dependence of our halo models. We note below when our inferences probe this unphysical regime.

Our halo models have three parameters: r_c and Λ_h determining the shape of the differential burst rate calculated from $\dot{n}(\mathbf{r}, \Lambda)$, and $\dot{n}_0$ determining its amplitude. As in Paper II, it proves convenient to replace some of these parameters with dimensionless parameters (some observable properties actually depend only on the values of the dimensionless parameters). The observable properties of a Galactic halo depend on the distance from Earth to the Galactic center, r_0. This distance is not known precisely but is generally found to be 8 to 9 kpc. We thus write $r_c = \rho_c r_0$, replacing the core size parameter with ρ_c. We also replace Λ_h with a dimensionless parameter, ν_h, defined so that

$$\Lambda_h = \nu_h 4\pi r_0^2 \Phi_{\mathrm{fid}}, \tag{3}$$

where Φ_{fid} is a fiducial peak photon number flux value which we set equal to 1 cm^{-2} s^{-1} (near the BATSE detection limit). With this definition, $\nu_h^{1/2}$ is the distance at which a burst source produces a burst with flux Φ_{fid}, in units of r_0. To simplify interpretation of our results, when plotting functions of ν_h, we provide an axis labeled with values of $r_{\mathrm{fid}}/r_0 = \nu_h^{1/2}$.

Several properties of the halo population depend only on the dimensionless parameters. But to infer the central burst rate density, we must fix r_0. We use the IAU recommended value of 8.5 kpc (recent estimates favor the somewhat smaller value of $R_0 = 8.0 \pm 0.5$ kpc; see Reid 1993). To adjust our inferred values of the central rate density to correspond to other choices of r_0, one would simply replace $\dot{n}_0$ with $\dot{n}_0 (r_0/8.5 \text{ kpc})^{-3}$.

To calculate the effects of a halo around M31, we place the center of M31 at a Galactocentric radius of $r_A = 78.82 r_0$, corresponding to $r_A = 670$ kpc when $r_0 = 8.5$ kpc (Allen 1973; Reid 1993 notes more recent values are as high as 760 kpc). We presume the M31 halo to have the same parameters as the Galactic halo, and thus its inclusion does not affect the number of parameters. We use the M31 position reported in the *Third Reference Catalog of Bright Galaxies* (de Vaucouleurs et al. 1991).

We number models consecutively from those studied in Paper II, and thus denote this dual halo model M_9.

The best-fit parameter values from separate analyses of the 64 ms and 1024 ms data appear in Table 1 with statistics comparing the models with standard candle cosmological models for the same data (model M_4 in Paper II). These statistics include the maximum likelihood ratio, $R_{9,4}$, and the Bayes factor, $B_{9,4}$. Since halo models and cosmological models are not nested, no simple frequentist method is available for comparing them (such as use of the asymptotic χ^2_ν distribution of $2 \log R$). The Bayes factor is not constrained to nested models, however, and permits an objective comparison of the models. One could calculate an approximate significance associated with the maximum likelihood ratio using Monte Carlo simulations, but we did not undertake this since we consider the Bayes factor to offer a more complete and accurate comparison of models.

We find that, for each data set, the best-fit halo model makes the data slightly more probable than the best-fit standard candle cosmological model ($R_{9,4} > 1$). But when account is taken of parameter uncertainty, the cosmological models are somewhat favored ($B_{9,4} < 1$). The 64 ms data favor cosmological models more strongly than the 1024 ms data; but neither data set decisively prefers one model to another.

To give some indication of how the anisotropy of these models affects the quality of the best-fit model, we constructed artificial isotropic models with $dR/d\Phi d\mathbf{n} = (1/4\pi)dR'/d\Phi$, where

$$\frac{dR'}{d\Phi} = \int d\mathbf{n} \, \frac{dR}{d\Phi d\mathbf{n}}, \tag{4}$$

The differential rate in the integral was that for the best-fit halo model. These models had likelihoods insignificantly larger than those of the anisotropic halos from which they were constructed: 2.7 times larger for the 64 ms data, and 1.5 times larger for the 1024 ms data (for reference, recall that a frequentist likelihood ratio test assigns 95% significance to a preference for a model with an additional parameter if the likelihood is increased by a factor of 7.4). Thus anisotropy is playing little role in assessing these models in the vicinity of the best-fit parameters. It plays an important role, however, in bounding the credible regions.

Figure 1 displays contours of the joint posterior density for the shape parameters resulting from analyses of the 64 ms (Fig. 1a) and 1024 ms (Fig. 1b) data. Crosses indicate the best-fit parameter points. The best-fit core radius and luminosity for the 64 ms data are nearly three and ten times larger than those for the 1024 ms data, respectively. But the 95% credible regions overlap significantly, so the difference between the best-fit values of the shape parameters exaggerates the discrepancy between the shapes of the differential rates required to model the data sets in the context of these models.

The vertical and horizontal dotted lines in Figure 1 indicate where the core size or fiducial distance equals r_A. Our models should be considered physically implausible at scales of order half this or larger, as noted above. In particular, the second mode evident in Figure 1a at large ν_h and ρ_c corresponds to models that effectively consist of a single gigantic halo enclosing both

the Galaxy and M31, a physically implausible model. We could have eliminated this behavior by making the prior vanish in these implausible regions, but instead left the prior nonzero in order to display the behavior of the likelihood function in various extreme parameter regimes (discussed further below).

The credible regions based on the 1024 ms data are significantly narrower than those based on the 64 ms data. This is due in part to the larger number of bursts observed on the 1024 ms timescale. In addition, in Paper II we showed that there is significant evidence for steepening of the distribution of 1024 ms peak fluxes for $\Phi \gtrsim 30$ cm^{-2} s^{-1}. Hence the fit to the 1024 ms data will be improved if the bright bursts are observed from distances $\lesssim r_c$ (where the burst distribution begins to resemble a homogeneous distribution), and this may be partly responsible for making the posterior calculated from the 1024 ms data narrower than that calculated from the 64 ms data. Only models with a more flexible flux distribution (such as the broken power law models studied in Paper II) reveal discrepancies between the two data sets.

The credible regions for both data sets have several common features: values of r_c and $r_{\rm fid}$ smaller than r_0 are excluded, as are values $\gtrsim r_A/2$ (except for the a priori implausible upper right region of Fig. 1a, mentioned above); and in the allowed region of parameter space, the inferred core radius and burst luminosity are strongly and positively correlated. We can understand these features as follows (Hakkila et al. 1994 also discuss some of this qualitative behavior).

First, consider models with small cores, $r_c \lesssim r_0$ (i.e., $\rho_c \lesssim 1$). When $r_{\rm fid} \gtrsim r_0$ (i.e., $\nu_h \gtrsim 1$), the observable bursts are significantly concentrated toward the Galactic center; such models are excluded because of the apparent isotropy of the distribution of 3B burst directions. When $r_{\rm fid} \ll r_0$ (i.e., $\nu_h \ll 1$), the visible part of the halo instead appears nearly isotropic and homogeneous. Although the observed distribution of directions is nearly isotropic, the observed distribution of burst peak fluxes falls less quickly with Φ than the $dR/d\Phi \propto \Phi^{-5/2}$ behavior predecited by a homogeneous population (see, e.g., § 4 of Paper II), so these models, too, are excluded. Finally, when $r_{\rm fid} \gg r_0$, the peak flux distribution is dominated by the $1/r^2$ part of the halo, which results in $dR/d\Phi \propto \Phi^{-3/2}$. The observed distribution falls more quickly than this (see, e.g., § 4 of Paper II). Thus all models with $r_c \lesssim r_0$ are excluded, accounting for the empty lower region of Figure 1.

Now consider models with large cores, so that $r_c \gg r_0$ (i.e., $\rho_c \gg 1$). When $r_{\rm fid} \ll r_c$ (i.e., $\nu_h \ll \rho_c$), the BATSE data sample the halo distribution from within its characteristic length scale, producing a visible distribution that is nearly isotropic and homogeneous. As just discussed, the homogeneity of such a population is inconsistent with the data, so these models (to the left of the credible regions in Figure 1) are excluded. When instead $r_{\rm fid} \gg r_c$, the observable bursts are approximately sampled from a $1/r^2$ distribution. The flux distribution associated with such a radial distribution is $dR/d\Phi \propto \Phi^{-3/2}$. This flux distribution falls more rapidly than is indicated by the data, and thus models to the right of the contours are excluded (see § 4 of Paper II).

Thus only models with $r_c \gg r_0$, and $r_{\rm fid} \gtrsim r_c$ are viable, hence the strong positive correlation.

In fact, the posterior is aligned parallel to the line $r_c = r_{\mathrm{fid}}$.

Finally, the constraint at jointly large values of r_{fid} and r_c is due to the M31 halo becoming too prominent in this part of parameter space. The dotted lines in Figures 1a and 1b indicate where $r_c = r_A$ and $r_{\mathrm{fid}} = r_A$, and intersect just beyond the credible regions (for the 64 ms data, very large halos that are significantly larger than r_A are also formally viable, although they are physically implausible). To further demonstrate the importance of including M31 to constrain this region of parameter space, we recalculated the joint posteriors without the M31 halo. Credible regions for these purely Galactic models appear in Figure 2. They do not close at large values of ν_h and r_c.

The constraint on models with large luminosities ($r_{\mathrm{fid}} \gg r_c$) is the only constraint that arose due to the distant $1/r^2$ falloff of the halo density. If the falloff is less rapid, the constraint is weakened. To illustrate this, we studied a model with $\dot{n}(r) \propto 1/(r + r_c)$. For such a model, when $r_c \gg r_0$ and $r_{\mathrm{fid}} \gg r_c$, the flux distribution is approximately $dR/d\Phi \propto \Phi^{-2}$. As we showed in our study of power law flux distributions in § 4 of Paper II, a Φ^{-2} power law adequately describes the distribution of 64 ms peak fluxes and of all but the brightest 1024 ms peak fluxes. Thus we expect large luminosity models *not* to be ruled out for $1/(r + r_c)$ halo models. In Figure 3, we show contours of the joint posterior for ν_h and ρ_c for such a model, based on the 1024 ms data. As expected, the credible regions have opened up at large ν_h compared to those in Figure 1. But we consider these models to be of only academic interest; we know of no compelling physical argument that leads to $\dot{n}(r) \propto 1/(r + r_c)$.

The 95% credible regions for the shape parameters derived from both data sets overlap considerably. This may seem to imply that the two data sets are consistent with each other, but such a conclusion is unjustified without examining the entire parameter space, including the amplitude parameter, $\dot{n}_0$, that we integrated over to obtain the marginal distribution for the shape parameters. Figure 4a shows contours of the joint distributions for ν_h and $\dot{n}_0$, conditional on the best-fit values of ρ_c for each data set. The regions allowed by the two data sets lie far from each other. The two data sets imply quite different best-fit values of ρ_c, however; Figure 4a thus displays "slices" of the three-dimensional posterior taken in different planes for each data set. Figure 4b instead shows contours of the posteriors conditional on $\rho_c = 10$, a value lying inside the 95% credible regions for each data set. The credible regions now lie closer together; in particular, were we to project or integrate the distributions along either axis, they would overlap substantially. However, Figure 4b makes it clear that the full posteriors are disjoint, the nature of the discrepancy being that for any given values of the luminosity and core size, the 64 ms data imply a burst rate density over 50% larger than that implied by the 1024 ms data. We found similar behavior in our study of cosmological models in Paper II, and noted there that such behavior could easily arise if bursts have peaks substantially briefer than 1024 ms, so that the peaks are "diluted" when measured on this timescale. Further discussion appears in § 6 of Paper II.

3.2. Models With Power Law Luminosity Functions

In their study of Galactic halo models, Hakkila et al. (1995) concluded that models with power law luminosity functions that span a dynamic range greater than about 5 are incompatible with the BATSE data. If true, we would consider this an argument *against* halo models. Given the extreme diversity of burst temporal behavior, and the broad diversity of burst spectra, it seems highly unlikely to us that the burst phenomenon has a single standard luminosity or a very narrow luminosity function. Thus we would consider incompatibility of broad luminosity functions with the BATSE data to be evidence that the success of standard candle halo models is fortuitous. We have therefore sought to verify the conclusion of Hakkila et al.. Our study is guided by our analysis of cosmological models with broad luminosity function in Paper II. There we found that the constraint on cosmological luminosity functions reported by Hakkila et al. (1994) was incorrect; they reported that power law luminosity functions had to have a dynamic range less than about 10, whereas we find the dynamic range to be completely unconstrained. We gave a simple and intuitive explanation of the lack of a constraint in § 5.3 of Paper II. Similar arguments should apply here, except that the presence of M31 could possibly complicate matters. In fact, we find that for halo models, too, the dynamic range of a power law luminosity function is not constrained by the data.

We now consider models with a bounded power law luminosity function, so that in the interval $[\Lambda_l, \Lambda_u]$ the burst rate density is

$$\dot{n}(\mathbf{r}, \Lambda) = \dot{n}(\mathbf{r}) \, A \Lambda^{-p}, \tag{5}$$

with $\dot{n}(\mathbf{r})$ given by equation (2), and A a normalization constant determined by p, Λ_l, and Λ_u. Outside of the luminosity interval, the burst rate density vanishes.

To calculate the differential burst rate implied by equation (5), we must perform an integration over Λ, as well as the radial integral required to calculate the differential rate for standard candle models. Since calculation of the likelihood function requires numerous three-dimensional integrals of the differential rate, the extra integration dimension makes analysis of models with luminosity functions computational burdensome. We thus have not explored the full parameter space of this model, and we cannot report a Bayes factor for it. The study of Hakkila et al. (1995) is similarly constrained.

We use the qualitative features of models with luminosity functions, together with some of the findings of Paper II, to guide our restricted search of parameter space. In particular, we fix the power law index, p, based on knowledge of the behavior of the flux distributions implied by power law luminosity functions, and the the slope of the flux distribution implied by the data and inferred in § 4 of Paper II. As we noted there, it is simple to show that a bounded population that vanishes beyond radius r_c implies a differential flux distribution proportional to $\Phi^{-5/2}$ for bursts with fluxes brighter than $\Lambda_u/(4\pi r_c^2)$, and proportional to Φ^{-p} for dimmer bursts. The flux distribution thus mimics the luminosity function below the flux corresponding to observing the brightest bursts at the boundary of the distribution. The flux distribution vanishes below

$\Lambda_l/(4\pi r_c^2)$, the flux of the dimmest bursts at the boundary.

Halo models complicate this picture in three ways: the boundary is not "hard," the distribution falls like $1/r^2$ beyond r_c; we are offset from the geometric center of the distribution, leading to anisotropy; and the halo around M31 introduces further anisotropy and changes the flux distribution for distant bursts. To guide our choice of parameters, we focus on the flux distribution, and consider the properties of a single halo observed from its center. A simple analytic calculation, described in Appendix B, reveals the generic behavior plotted in Figure 5 for the parameter range of interest in studying bursts. At large fluxes, $dR/d\Phi \propto \Phi^{-5/2}$, the familiar power law associated with a homogenous population. Going to lower fluxes, the differential rate first flattens to $dR/d\Phi \propto \Phi^{-p}$ at a flux of $\Lambda_u/4\pi r_c^2$, and then flattens further to $dR/d\Phi \propto \Phi^{-3/2}$ below a flux of $\Lambda_l/4\pi r_c^2$. The dynamic range for the Φ^{-p} behavior is Λ_u/Λ_l.

As discussed in Paper II, there is no evidence that BATSE has yet observed the $\Phi^{-5/2}$ behavior expected for bright bursts (although there may be evidence for much more significant steepening in the 1024 ms data). In the context of models with luminosity functions, the observed data must span part of the Φ^{-p} and $\Phi^{-3/2}$ regions. In this case, the simple calculation that produced Figure 5 indicates that the dynamic range of a luminosity function with index p can be constrained only if the differential flux distribution flattens from Φ^{-p} to $\Phi^{-3/2}$ over the range of the data. No such flattening is visible to the eye in the "complete" portion of the data (above $\Phi = 3$ cm^{-2} s^{-1} for the 64 ms data, or $\Phi = 1.5$ cm^{-2} s^{-1} for the 64 ms data). But it remains possible that the flattening due to the efficiency function is hiding some intrinsic flattening, or that the complications due to our offset from the Galactic center and the presence of M31 produce characteristics in the joint distribution of fluxes and directions that yeild a constraint.

Accordingly, we investigated models with $p = 1.8$, and with a dynamic range of 10^3. We chose $p = 1.8$ because we found that both phenomenological and cosmological models with $\Phi^{-1.8}$ low-flux behavior fit both data sets well in Paper II. The dynamic range of 10^3 is many times larger than the upper limit of 5 found by Hakkila et al., and is a value that we showed to be consistent with the data in the context of the isotropic models studied in Paper II. With these parameters fixed, only two shape parameters remain: the core radius parameter, ρ_c, and the upper limit of the luminosity function, Λ_u. As with standard candle models, we introduce a dimensionless parameter, ν_u, for the luminosity, defined so that

$$\Lambda_u = \nu_u 4\pi r_c^2 \Phi_{\mathrm{fid}}. \tag{6}$$

Figure 6a shows plots of the logarithm of the shape parameter likelihood as a function of ν_u, when ρ_c is fixed at the most probable value found from the previous analysis of *standard candle* models ($\rho_c = 18.1$ for the 64 ms data; $\rho_c = 7.8$ for the 1024 ms data). Curves are shown both for the 64 ms (solid) and 1024 ms (dashed) data. The likelihoods have been divided by the maximum likelihoods for the corresponding best-fit standard candle models. For the 64 ms data, models with $\nu_u \approx 7000$ are actually slightly superior to standard candle models, so it is clear that the 64 ms data allows luminosity functions with a dynamic range of at least 10^3. On the other hand,

the best model for the 1024 ms data has a likelihood almost 40 times lower than that of the best standard candle model for these data. This would seem to indicate a reasonably strong preference for narrow luminosity functions for these data. In fact, Hakkila et al. (1995) studied 1024 ms data (although they used *energy* flux data, not photon number flux data).

However, Figure 6a constrains ρ_c to its standard candle best-fit value. Although we have not performed a full study of the (ρ_c, ν_h) parameter space, Figure 6b presents results similar to those shown in Figure 6a, but with slightly reduced values of ρ_c ($\rho_c = 10$ for the 64 ms data; $\rho_c = 5$ for the 1024 ms data). The likelihoods for both 64 ms and 1024 ms models have improved. In fact, the likelihood for the best 1024 ms model is now only 2.7 times smaller than that of the best standard candle model, and is clearly acceptable. It is likely that futher adjustment of ρ_c or of p would improve the likelihood further. Thus models with *very* broad luminosity functions are entirely consistent with the data, and are competitive with both standard candle halo models and cosmological models.

Hakkila et al. (1995) offer very few details about their study, but do note that they explored luminosity function models only with parameters in the vicinity of the best-fit standard candle models. The core radii for the acceptable models in Figure 6b are lower than those of acceptable standard candle models, and the luminosity upper limits are significantly higher than the luminosities of acceptable standard candle models. We suspect that an unnecessarily restrictive study of the parameter space is responsible for the different conclusions of Hakkila et al. (1995).

3.3.   The Anisotropy of Halo Models

Some of our findings may appear somewhat surprising in the light of simple arguments regarding the anisotropy of halo models. Hartmann (1994) and Hartmann et al. (1994) point out that a Galactocentric shell of radius r has a dipole moment $D = \langle \cos\theta \rangle$ given by

$$D(r) = \frac{2}{3}\frac{1}{\rho},\tag{7}$$

where $\rho = r/r_0$. Arguing that any spherically symmetric halo model may be thought of as the weighted sum of a series of such shells, they use equation (7) to constrain the length scale of halo models. Briggs et al. (1994) use this result, finding that shells with $r < 110$ kpc have dipole moments inconsistent with the dipole moment of the proprietary sample of 1005 bursts that they analyze. They argue that any bursts interior to this radius must be balanced by those exterior to it, implying that only models with very large length scales will be acceptable. Whether the argument is meant to constrain the core size or the distance to the faintest sources is not clear.

In contrast to this argument, we find that models with core sizes as small as $2r_0 = 17$ kpc and with bursts visible only out to ≈ 50 kpc lie within the 95% credible region for standard candle models for the 1024 ms data; both scales are substantially smaller than the ~ 100 kpc scale identified by the Galactocentric shell argument. We are analyzing a smaller data set than is

available to Briggs et al. (1996); but their own analysis of specific models also identified acceptable models with length scales very much smaller than the ≈ 100 kpc scale. The Galactocentric shell argument has been so widely cited that these results certainly deserve some comment.

In fact, this argument is misleading because it fails to distinguish the artificial anisotropy arising from the displacement of the centers of Galactocentric shells from the observing point (the Sun), and the actual, intrinsic anisotropy best quantified by calculating angular moments of shells centered on the Sun. The simplest way to see this is to consider observations of a completely homogeneous population. Of course, the observed dipole moment of such a population has an expectation value of zero, not only for the entire data set, but also for every constant-Φ subset. In this case, the dipole moments of the Galactocentric shells considered in the argument of Hartmann et al. (1994) are entirely an artifact of their offset from the observing point. A vanishing moment cannot be realized by any positively weighted superposition of D values given by equation (7), but certainly a proper treatment of the observation of such shells must produce a vanishing dipole moment. The way this comes about is elucidated by Figure 7, which shows cross sections of a large-r Galactocentric shell, and of a Sun-centered shell which we take to have nearly the radius at which the dimmest observable bursts lie. Near the observing limit, the dipole moments of the *observable* part of Galactocentric shells are *negative*, because only those parts of the shells in the direction of the anticenter (highlighted) are visible. These negative contributions cancel the positive moments of smaller shells that are completely visible, so the total dipole moment vanishes. This effect is ignored in the argument of Hartmann et al. (1994) and Hartmann (1994).

Hartmann et al. (1994) sought to constrain the length scale of the burst population in a manner that was both model-independent and avoided complications due to observational selection effects. Their focus on Galactocentric shells achieved model independence in that all models that are spherically symmetric about the Galactic center can be built by superposing such shells. But the offset of the shells from the Sun makes consideration of selection effects crucial for calculating observed moments, and seriously complicates any discussion of the intensity dependence of the expected anisotropy. A model will predict anisotropy in the burst data as a whole only if shells centered on the Sun exhibit anisotropy. Unfortunately, the anisotropy of such shells depends on how the burst rate density varies with Galactocentric radius. We therefore find it difficult to see how one could actually constrain length scales of spherically symmetric halo models in a model-independent manner.

If we forsake model independence, we can gain some insight into why halo models with distance scales smaller than ~ 100 kpc are acceptable by calculating the dipole moments of shells of radius r' from the Sun, assuming the standard halo profile used above. A straightforward analytic calculation, described in Appendix C, shows that a good approximation is

$$D(r') \approx \frac{2}{3} \frac{1}{\rho' + \rho_c + \frac{1}{\rho'}}, \tag{8}$$

where $\rho' = r'/r_0$ and $\rho_c = r_c/r_0$. Comparing with equation (7), we see that a Solar-centric shell of a given size has a dipole moment that is always smaller than that of a Galactocentric shell

of the same size. Also, in stark contrast to the Galactocentric case, Sun-centered shells with small r' have *small* dipole moments, because they are observed across a region over which the distribution appears homogeneous. The dipole moment takes its maximum value for $\rho' \approx \sqrt{\rho_c + 1}$; small observed moments can result from populations observed predominantly at distances *smaller* than this, as well as from those with many distant bursts. Finally, in contrast to equation (7), equation (8) clearly displays the distinct roles played by the two distance scales: the observing distance, r', and the core size, r_c. These characteristics of $D(r')$ make feasible the acceptability of models with distance scales smaller than 100 kpc; but only a rigorous, model-dependent statistical analysis can produce quantitative constraints.

It may also appear surprising that the likelihood of models with luminosity functions is improved by *decreasing* the core radius below that of standard candle models, presumably increasing their anisotropy. Such behavior was noted in passing by Brainerd (1992), but left unexplained. Figures 8 and 9 elucidate the reason for this somewhat counterintuitive behavior. Figure 8a shows the burst rate (per unit distance) as a function of radius from the Sun, r', for the standard candle model that best fits the 1024 ms data. The burst rate per unit distance was calculated according to

$$\frac{dR}{dr'} = r'^2 \int d\mathbf{n}\, \dot{n}(\mathbf{r}) \int d\Lambda\, f(\Lambda)\bar{\eta}\left(\frac{\Lambda}{4\pi r'^2}, \mathbf{n}\right),$$ (9)

where $f(\Lambda)$ is the luminosity function (a δ-function for standard candle models), and $\bar{\eta}(\Phi, \mathbf{n})$ is the time-averaged efficiency for detecting bursts of flux Φ from direction $\mathbf{n}$. As a simple qualitative measure of the anisotropy of the burst population, Figure 8b shows the dipole moment, D (the average of the cosine of the angle between a burst and the unit vector to the Galactic center), of a shell of a given radius. It is slightly negative at small distances due to the slightly negative dipole moment of the BATSE sky exposure map; it is negative at large distances due to M31, which is in the hemisphere opposite of the Galactic center. Figures 8c and 8d show similar results for the best broad luminosity function model we studied for the 1024 ms data, a model with $p = 1.8$, $\rho_c = 5$, $\nu_u = 2 \times 10^3$, and a dynamic range of 10^3. As expected, according to this model the bursts are observed from smaller distances than in the best standard candle model, and have significantly larger anisotropy on constant-radius shells.

In contrast, Figure 9 shows the dipole moments for these models as functions of *peak flux* rather than of radius; Figure 9a is for the standard candle model and Figure 9b is for the model with a broad luminosity function. Also shown are the dipole moments (with statistical error bars) of the best-fit burst positions for bursts in five flux bins of equal logarithmic width. Although the luminosity function model exhibits a larger dipole moment than the standard candle model at all fluxes, its dipole moment is significantly lower at all fluxes than its maximum value in the D vs. r/r_0 plot of Figure 8d. Further, it peaks at larger fluxes than does the standard candle curve. There are fewer bursts at these fluxes than at lower fluxes, and thus weaker constraints on anisotropy, as the error bars illustrate (the data also slightly favor large dipole moments at large fluxes). Due to the broad luminosity function, the bursts from a shell with a large dipole moment

appear at a wide variety of fluxes, mixed with bursts seen from other shells with less anisotropy. The luminosity function thus "spreads" the anisotropy out over a large range of fluxes, allowing populations with smaller core radii to fit the data.

4. Two-Population Models

4.1. Motivation

Many authors have noted the bewildering variety of characteristics exhibited by GRBs, particularly in regard to their temporal behavior. Some investigators have regarded this variety as evidence that GRBs are not due to a single underlying phenomenon, and this possibility has motivated many attempts to classify bursts according to their temporal or spectral properties. Several such attempts predate the BATSE observations, but no consensus was reached on the number or defintions of burst classes (see the reviews of Hurley 1986 and Higdon and Lingenfelter 1990 for further discussion).

The large and uniform data base provided by BATSE offers new opportunities for burst classification. The most intriguing finding so far reported is the discovery of suggestive evidence for two classes of bursts distinguished by light curve morphology: Lamb, Graziani, and Smith (1993) identify two classes based on a simple measure of light curve variability; Kouveliotou et al. (1993) instead identify two classes based on simple measures of burst duration. The statistical significances of these discoveries are difficult to determine, due to both ambiguity in modeling the classes and the possibility of subtle effects mimicking the signatures of distinct classes for certain measures of light curve morphology (see, e.g., Wang 1996). Both groups of investigators find that class membership is correlated with other burst properties (such as hardness or brightness), and some recent studies find supporting evidence in larger data sets (Kouveliotou et al. 1996; Katz and Canel 1996). This may support the reality of the classes, although a correlation between temporal and other properties could arise from a single underlying mechanism.

Two somewhat more controversial discoveries also suggest that there may be two or more classes of bursts. As noted in § 1, the *Ginga* experiment discovered strong evidence for the presence of low-energy absorption-like features in about 20% of the bursts it observed. Such bursts may constitute a distinct class, and in the best-studied models for the formation of the features—the cyclotron scattering model mentioned in the Introduction—the sources of these bursts would have to lie within several hundred parsecs of the Sun if the scattering region is gravitationally confined. The distribution of burst intensities is not compatible with such a distribution, so bursts without features would presumably have a very different (perhaps cosmological) spatial distribution. BATSE has yet to confirm the presence of such features in bursts, but the present limits and candidate features are not inconsistent with the *Ginga* results (Palmer et al. 1994; Band et al. 1994, 1995; Briggs et al. 1996), and there are some questions regarding how well BATSE could detect such features (Band et al. 1995; Paciesas et al. 1996; Freeman et al. 1996). The small

number of bright bursts observed by *Ginga* results in large uncertainty in the inferred fraction of bursts with such features, but it is interestingly similar to the size of the smaller of the two classes inferred from light curve morphology. In addition, several investigators reported suggestive evidence for burst repetition based on clustering of the burst directions reported in the 2B catalog (Lamb; Wang and Lingenfelter). Only a small subset of bursts exhibited clustering; these may comprise a distinct class. The evidence for repetition is absent in the 3B catalog (Hartmann et al. 1996; Luo, Loredo, and Wasserman 1996; Luo and Wasserman 1996), but the directions reported in this catalog were calculated with a new burst direction algorithm that has systematic errors that appear to be significantly more complicated than those in the 2B catalog (Graziani and Lamb 1996); the additional complications have yet to be fully characterized or incorporated in searches for evidence of burst repetition.

Although none of the observational studies just described is completely compelling, together they suggest that one take seriously the possibility that bursts arise from two or more populations with distinct characteristics. Some theoretical studies also suggest that bursts might be produced by distinct phenomena that are observable at different spatial scales. For example, Wasserman and Salpeter (1995) have suggested that the universal behavior exhibited by the rotation curves of galaxies may indicate the presence of a baryonic halo around galaxies consisting of stellar remnants of various types resulting from the evolution of a population of stars produced prior to the collapse of the protogalaxy. They have calculated various collision rates for these remnants, and they identify two types of collisions that are energetically plausible sources of bursts and that might produce bursts at roughly the rate observed. Collisions between neutron stars and asteroids could produce bursts observable throughout the halo of the Galaxy at rates $\sim 10^2$ yr^{-1}. Collisions between pairs of neutron stars (not in binary systems) could produce bursts observable to cosmological distances at a similar rate. In this picture, bursts thus arise from both a local halo population and a cosmological population of sources. Katz (1996) envisions a scenario that similarly divides burst sources into local and cosmological components, the former due to magnetic reconnection in neutron star magnetospheres, and the latter due to the interaction of a fireball (possibly produced by a collision between a neutron star and a companion neutron star or black hole) with surrounding clouds, as suggested by Shemi and Piran (1990) and Mészáros and Rees (1993).

These observational and theoretical arguments have motivated us to study two-population models for burst sources comprised of a local halo population and a cosmological population. More pragmatically, such models are interesting to study simply because they provide a convenient framework in which we can place precise (but model-dependent) constraints on the fraction of bursts in a local, anisotropic population. Of course, since we have already demonstrated that pure halo models and cosmological models can independently account for the data equally well, we know that one can create successful two-population models with any desired fraction of bursts in the local population. However, here we restrict the halo population to reside in *Bahcall-Soneira halos with a 2 kpc core*. These halos have $\rho_c = 0.235$, and are thus *not* acceptable by themselves.

However, it is widely believed that a dark matter halo with a core size similar to this exists, on the basis of Galactic rotation curve measurements. Further, this halo scale is similar to that of the baryonic halos studied by Wasserman and Salpeter (1995). Thus, unlike the halos of the previous section, the halos we study here are not created solely for the purpose of hosting bursts.

Finally, these models are also of interest in that they offer a model-dependent test of the adequacy of cosmological models: even if one rejects these models as subjectively implausible a priori, if models with a substantial halo component have higher likelihoods than purely cosmological models, this could indicate that the data prefer more complicated alternatives to the cosmological models we studied in Paper II. Whether the improvement is due to slight anisotropy or improved fitting of the flux distribution could offer clues as to which alternatives one might study.

4.2. Model Specification

For the cosmological component, we consider a distribution of standard-candle burster sources in a $\Lambda = 0$, $\Omega_0 = 1$ universe. This model is discussed in detail in Paper II (Model M_4 of § 5.1). This model component has a single shape parameter, the standard candle photon number luminosity, Λ_c. We write Λ_c in terms of a dimensionless luminosity, ν_c, according to

$$\Lambda_c = \nu_c (4\pi c^2 / H_0^2) \Phi_{\text{fid}} K(0), \tag{10}$$

where H_0 is Hubble's constant, $K(z)$ is a redshift-dependent spectral correction function (similar to a "K-correction"), and Φ_{fid} is a fiducial value of the observed flux, which we set equal to 1 cm^{-2}s^{-1}. For $\nu_c = 1$, $\Lambda_c \approx 10^{57}$s^{-1}, corresponding to a luminosity of approximately 10^{51} erg s^{-1} for $H_0 = 100$ km s^{-1}, and burst sources with $z \approx 1$ for bursts with $\Phi \approx 1$. The best-fit value of ν_c in a purely cosmological model is $\nu_c \approx 0.4$ for both the 64 ms and 1024 ms data. We note that cosmological models with density evolution or with luminosity functions studied in Paper II do not substantially improve on standard candel models. Thus although this model is simple, it is representative of all successful cosmological models for the 3B data.

For the local component, we consider a dark matter halo distribution of standard-candle sources with the core radius fixed at $r_c = 0.235 r_0 = 2$ kpc. As noted above, this choice thus corresponds to associating local bursters with a known distribution of matter in the Galaxy. A single shape parameter describes the flux distribution resulting from such a population: the standard candle photon number luminosity, Λ_h. As in the previous section, we write this luminosity in terms of a dimensionless parameter, ν_h, according to equation (3). As shown below, the only tenable models have values of ν_h small enough that the contribution of an M31 halo would be completely negligible. We thus omitted the M31 halo from the calculations, to speed them up.

The full two-component model combines the cosmological and halo populations so that a fraction, f, of the observable bursts comes from the halo population. The model thus has three

shape parameters, the two luminosity parameters, ν_c and ν_h, and the halo fraction, f. Note that since f parametrizes the fraction of *observable* bursts in the halo component, its meaning depends on the instrument providing the data being analyzed. In particular, its meaning is different for the 64 ms and 1024 ms timescale data sets.

4.3. Results

Figure 10 shows the profile likelihood as a function of the halo luminosity, ν_h. The profile likelihood for a subset of a model's parameters is simply the likelihood maximized over the remaining parameters; it is sometimes a good approximation to the marginal distribution for the subset of parameters. Here we use it simply as a convenient display of some of the features of the full joint posterior. The profile likelihood reveals the posterior to be multimodal, with (at least) one mode in the region where $\nu_h \gg 1$ (corresponding to sources more distant than the Galactic center) and another where $\nu_h \ll 1$ (sources much closer than the Galactic center). We thus examine models with dim ($\nu_h < 1$) and luminous ($\nu_h > 1$) halo burst sources separately. The 1024 ms data imply a third small mode for $\nu_h \approx 1$; such solutions are inconsistent with the 64 ms data, although we do discuss them briefly below.

4.3.1. Models With Luminous Local Bursters

Table 2 presents the best-fit parameters for models with luminous halo bursters based on both data sets. Also listed are the ratios of the best-fit likelihoods to those of the best-fit standard candle cosmological models (corresponding to $f = 0$), and the Bayes factors favoring two-population models with $1 < \nu_h < 10^3$ over standard candle cosmological models. The Bayes factors were calculated with a relatively crude grid in ν_h, and are probably accurate to only one significant figure.

The Bayes factors are not significantly different from unity, indicating no strong preference for or against these models over purely cosmological models, once account is taken of the unknown parameters. Since purely cosmological models are nested within our two-component models, we can also easily calculate calculate the significance associated with a frequentist likelihood ratio test (this was not possible for the pure halo models studied above). Table 2 lists the probability $p(> R)$ of seeing a larger maximum likelihood ratio, presuming the best-fit cosmological model is true). The table lists approximate significances, calculated using the asymptotic χ_2^2 distribution of $2 \log R$. This approximate frequentist test agrees with the Bayes factor in the sense that it does not find the preference for two-component models to be very significant. The Bayes factor is a more complete comparison; it accounts for the sizes of the parameter spaces of the models, comparing the *average* rather than maximum likelihoods, and thus implementing an automatic and objective "Ockham's Razor."

The best-fit halo luminosities imply a local population visible to ≈ 50 kpc ($r_{\rm fid} = 49.8$ and 37.1 kpc for the 64 ms and 1024 ms best-fit parameters). The cosmological luminosities are significantly smaller than unity, implying a cosmological component that is nearly homogeneous over the span of the 3B data. These ν_c values are significantly smaller than the values of order unity favored in purely cosmological models.

Figure 11 shows contours of the joint distribution for the observable halo fraction, f, and the cosmological luminosity, ν_c, conditional on the best-fit values of ν_h for each data set (listed in Table 2). (The joint marginal distributions will be somewhat wider after averaging over ν_h, but not significantly so because correlations with ν_h are weak.) Halo fractions of order 10% are favored, and surprisingly large values of f can be tolerated: models with $f \approx 0.2$ lie within the 95.4% credible regions. Thus halo fractions consistent with the sizes of the burst classes hypothesized in the studies reviewed above are consistent with the 3B data.

We constructed isotropic versions of the best-fit models in the manner discussed above (see eqn. (4)) and calculated their likelihoods. The isotropic versions had likelihoods that were very slightly larger (factors of 1.22 and 1.12 larger for the 64 ms and 1024 ms data, respectively). The anisotropy of these models is playing little role in determining the quality of the best-fit model. We can thus understand the best-fit models by focusing on their predicted intensity distributions.

In Figure 12 we show the cumulative distributions of burst fluxes predicted by the best-fit models, along with the observed cumulative histograms. The dashed curve (associated with the right axis) shows the negative logarithmic slope of the cumulative distribution. These models are more successful than purely cosmological models because the halo component allows the differential rate to steepen more quickly with flux. Figure 13 shows the total differential rate (solid) and the separate differential rates for the cosmological (dotted) and halo (dashed) components of the best-fit models, illustrating how the steepening comes about. At low fluxes, the halo component differential rate is $\propto \Phi^{-3/2}$ and is small compared to the cosmological component. But above a flux of 10 to 20 cm^{-2} s^{-1}, the halo component quickly steepens to a $\Phi^{-5/2}$ power law, and is comparable in magnitude to the cosmological component. In this manner, the slowly flattening cosmological component accounts for the Φ^{-2} behavior exhibited by dim bursts, and both components together account for the bright bursts, whose rate falls off more steeply. The halo component not only makes the change to $\Phi^{-3/2}$ behavior more abrupt; it also somewhat enhances the number of bursts at large fluxes. This enhancement appears as a small bump in the total differential rate in Figure 13; it is not apparent in the cumulative distribution.

4.3.2. Models With Dim Local Bursters

Table 2 also lists the best-fit parameters for models with dim ($\nu_h < 1$) halo bursters based on both data sets, along with measures of the quality of fit of these models. For the 64 ms data, the likelihood is maximized for the smallest value of ν_h we examined, $\nu_h = 10^{-3}$. For the 1024 ms

data, there is a definite mode at $\nu_h \approx 10^{-2}$, but the likelihood remains large for $\nu_h = 10^{-3}$. In both cases, the favored models have bursts visible only from within a kiloparsec from the Sun. The local component is thus nearly isotropic and homogeneous. The best-fit cosmological luminosity is significantly larger in these models than in models with a luminous local population. The cosmological component thus exhibits strong apparent inhomogeneity over the span of the 3B data.

The maximum likelihood is much larger than that of purely cosmological models; but again, the Bayes factor indicates that these models are neither decisively favored nor disfavored compared to simpler purely cosmological alternatives. We constructed isotropic versions of the best-fit models by averaging over direction, as described above. The likelihood of the isotropic version of the 64 ms best-fit model was greater than that of the actual anisotropic model by a small factor (4.3). The likelihood of the 1024 ms isotropic model is 2.5 times *smaller* than that of the anisotropic model. The small anisotropy of the local component actually helps this model, though by an insignificantly small amount. This is an interesting result, because it is not what one would conclude were one to consider only the dipole moment D, or the quadrupole moment $q = 1/3 - \langle \sin^2 b \rangle$. The moments for the 1024 ms data we are considering are $D = 0.0065 \pm 0.027$ and $q = -0.025 \pm 0.013$ (the quoted errors are statistical only; additional error due to burst direction uncertainty is negligible). The predicted moments for isotropic models (i.e., the moments of the sky exposure) are $D = -0.0127$ and $q = -0.0048$. The predicted moments for the best-fit two component model are $D = 0.022$ and $q = -0.0024$; each is further from the data than are the values predicted by isotropic models. Yet the anisotropic model has a larger likelihood than its isotropized version, presumably because the likelihood uses much more angular information than the dipole or quadrupole moments, including how the anisotropy varies with flux.

Figure 14 shows contours of the joint distribution for the halo fraction, f, and the cosmological luminosity, ν_c, conditional on $\nu_h = 0.01$. Very large halo fractions, of order 40 to 50%, are favored. Figure 15 shows the observed and predicted cumulative peak flux distributions, and Figure 16 shows the differential rates for the halo (dashed) and cosmological (dotted) components, as well as the total differential rate (solid). In contrast to models with luminous halo bursts, here the halo component is most important at *low* fluxes. Where the cosmological component flattens substantially at low fluxes, the $\Phi^{-5/2}$ halo component becomes important; the sum of the two components falls with roughly the Φ^{-2} behavior needed to fit the low-flux part of the intensity distribution. At large fluxes both components fall like $\Phi^{-5/2}$, the cosmological component dominating.

4.3.3. Intermediate Case

As noted above and displayed in Figure 10, the profile likelihood for ν_h based on the 1024 ms data exhibits a small mode at $\nu_h = 1.49$; for completeness we describe the properties of these solutions. The best-fit parameter values are $\nu_c = 0.46$, $\nu_h = 1.49$ (implying $r_{\text{fid}} = 10.4$ kpc), and

$f = 0.05$. Figure 17 shows contours of credible regions for f and ν_c, presuming ν_h equals its best-fit value. It has a shape and location intermediate to that exhibited by the dim and luminous models discussed above. Figure 18a compares the observed cumulative intensity distribution with that predicted by the best-fit model. Figure 18b shows the local, cosmological, and total differential rates. As is clear from these Figures, the local population plays a very minor role in these models. Interestingly, when we artificially isotropize this model, the likelihood *decreases* by a factor of 2.6. The anisotropy of the local component helps these models, though not significantly; in this respect they resemble the models with a dim local component.

5. Summary and Discussion

Our analysis of halo models in § 2 demonstrates that such models can account for the 3B data as successfully as cosmological models, provided one considers halos with core sizes significantly larger than those used to model the distribution of dark matter. Only a few years ago, a local population of sources with such a large characteristic size would have been considered highly implausible; such a population would have to have been hypothesized purely for the purpose of hosting bursts. We now know that there is a population of high velocity neutron stars that could conceivably provide a host population with a very large characteristic length scale. Whether the characteristics of such a population could model the burst data as successfully as the *ad hoc* halo models considered here is an open question, requiring detailed modelling beyond the scope of this study. Our work demonstrates how the analysis of such models can best be undertaken, and the results of § 2 should guide the study of other, more complicated local models.

The core sizes we infer are smaller than one might expect based on popular semiquantitative arguments that consider the superposed dipole moments of shells centered on the Galactic center (Hartmann et al. 1994; Briggs et al. 1994). Such arguments are misleading, as we show in § 2. They fail to distinguish the artificial anisotropy arising from the displacement of the centers of Galactocentric shells from the observing point (the Sun), and the actual, intrinsic anisotropy best quantified by calculating angular moments of shells at a constant radius from the Sun.

Our analysis of halo models also demonstrates that the 3B data do not constrain the width of power-law luminosity functions for burst sources. This result contradicts the findings of Hakkila et al. (1995), who used less rigorous analysis methods and who restricted their search of parameter space to a significantly smaller region than that explored here. We elucidate the qualitative reasons for the lack of such a constraint in § 2.

As with the isotropic models studied in Paper II, inferences based on the 64 ms and 1024 ms data are formally inconsistent, in the sense that there is negligible overlap of the credible regions found by analyzing the two data sets. Although the shapes of the burst distributions that best model each data set differ somewhat, the inconsistency arises largely because the two data sets imply very different burst rates per unit volume. The 64 ms data implies rates about 40%

larger than the 1024 ms data, and in this sense the 64 ms timescale is *more* sensitive than the 1024 ms timescale, even though the 1024 ms data set is larger (i.e., the 1024 ms data set is not as large as one would expect from extrapolating the 64 ms data set to the lower fluxes detectable using the 1024 ms timescale). In Paper II we argue that this difference could arise from "peak dilution" in the 1024 ms data set: when bursts have peaks briefer than 1024 ms, their intensities are underestimated by 1024 ms measurements. This changes the shape and normalization of the intensity distribution in a manner that may account for the discrepancy between the two data sets. The 64 ms data are not immune to such effects, but will be less affected.

We also studied two-population models, consisting of superposed standard candle cosmological and local halo populations. Numerous studies suggest that there may be two (or more) classes of bursts, as we review in § 3. These models also serve a purely pragmatic purpose of allowing precise, model-dependent quantification of the constraints the 3B data place on the anisotropy of the distribution of burst sources. They also provide a model-dependent test of the adequacy of cosmological models. For the two-population models, we took the halo population to follow the distribution of dark matter in a standard Bahcall-Soneira halo with a core size of 2 kpc, so that the local population is associated with a known distribution of matter. Two families of models successfully account for the data: models with luminous halo sources visible to ~ 50 kpc; and models with dim halo sources visible from within a disk scale height. Despite the fact that the luminous halo sources would be distributed anisotropically, models with $\approx 10\%$ of observable bursts from the halo are favored, and halo fractions as large as 20% are acceptable. Dim halo sources would comprise a nearly isotropic, homogeneous component. For such sources, the data favor large halo fractions, of the order of 40% to 50%. These results are consistent with the relative sizes of classes of bursts inferred from characteristics of burst lightcurves, or with the fraction of bursts observed by *Ginga* to have low energy absorption features. We have not yet ascertained whether membership in these classes is correlated with burst intensity in the manner that these models would predict.

The common methodology employed here and in Paper II, where we analyze cosmological models, permits us to rigorously compare how well cosmological and local models account for the full joint distribution of burst peak fluxes and directions. The Bayesian tool for this comparison—the Bayes factor—objectively accounts for parameter uncertainty, providing a quantitative "Ockham's Razor." We find that the data do not decisively prefer any one of the models we have studied to its competitors. In particular, local models and models with a substantial local component account for the 3B burst intensity and direction data as well as purely cosmological models.

Despite this, several investigators strongly prefer cosmological models to local ones, or vice versa. This preference can be justified only by consideration of information beyond that in the distribution of burst peak fluxes and directions analyzed here. Numerous studies have been undertaken of some additional burst characteristics, including searches for evidence of time dilation, burst repetition, and spectral lines. To date, such searches have been inconclusive, with

investigators who use different frequentist methodologies arriving at different, often conflicting conclusions. The Bayesian approach we have adopted in this work can be straightforwardly generalized to address many of these issues. Some such generalizations have already been outlined in Paper I, and we are pursuing studies of some of these outstanding controversial issues from within this framework.

A.   Constraining Model Parameters

In this work we have addressed questions about the adequacy of parameterized models. Statisticians using both frequentist and Bayesian methods have divided such questions into two classes. First is the class of *estimation* questions that assess the implications of assuming the truth of a particular model, usually by estimating values or allowed ranges for the model parameters. Second is the class of *model assessment* questions that assess the viability of a model. We have outlined Bayesian methods for treating these questions in Paper I and Paper II. A clear discussion of the application of frequentist methods for estimation and model assessment to problems in the physical sciences is available in the text by Eadie, et al. (1971).

The procedures used for estimation are fundamentally different from those used for model assessment. Unfortunately, the complexity of the GRB data makes the distinction between these problems somewhat subtle from the frequentist viewpoint, enough so that nearly every previously published statistical analysis of these data has inappropriately used model assessment procedures to address estimation problems. In particular, a number of studies used goodness-of-fit (GOF) procedures to specify "confidence" regions, usually based on the χ^2 or Kolmogorov-Smirnov (KS) GOF statistics. In these studies, the boundary of the calculated "confidence region" was determined by finding parameters for which the significance level of a GOF test is equal to the desired confidence level. Such misapplication of GOF procedures to parameter estimation problems is commonplace in astrophysics; we have been guilty of it ourselves in the past. Thus some discussion of the problems with this approach seems worthwhile.

To see the problems with such a procedure, it is instructive to apply this type of thinking in a context where the correct procedure is widely known. Consider, therefore, estimation and model assessment for a model with a single parameter, μ, using the χ^2 statistic. A common best-fit estimate for μ is the minimum χ^2 value, which we will denote by $\hat{\mu}$. A confidence region (CR) for μ is typically specified by reporting the region of μ for which χ^2 is less than some critical value, $\chi^2_{\mathrm{CR},P}$, found by adding to $\chi^2_{\min} = \chi^2(\hat{\mu})$ a fixed number, $\Delta\chi^2_P$, whose value is determined by the size of the confidence region desired:

$$\chi^2_{\mathrm{CR},P}(\hat{\mu}) = \chi^2(\hat{\mu}) + \Delta\chi^2_P. \tag{A1}$$

For example, for a 68% confidence region, $\Delta\chi_P^2 = 1$ (asymptotically). Note that the value of the critical χ^2 defining the region depends on the data (through $\hat\mu$).

Consider now the different problem of assessing the goodness-of-fit of some hypothesis that specifies a particular value of μ a priori; we denote this value by μ_0. For this problem, one typically finds the critical value, $\chi_{\text{GOF},P}^2$, such that one expects $\chi^2(\mu_0)$ to be less this value $100P\%$ of the time, presuming all model assumptions are true. By agreeing to reject the model if $\chi^2(\mu_0) > \chi_{\text{GOF},P}^2$, one will falsely reject a true model (i.e., commit a "Type I error") a fraction $(1-P)$ of the time. In contrast to the CR case, the critical value defining a GOF test is a constant that depends only on the number of the data, and not on the actual data values. It is simply the χ^2 value such that the probability for observing larger values from the χ_ν^2 distribution with $\nu = N$ is $(1-P)$; for example, for $P = 0.95$, $\chi_{\text{GOF},P}^2 = 43.8$ for $N = 30$. (If instead of an a priori μ value we wish to test the adequacy of the best fit model, we would compare $\chi_{\min}^2$ with a critical value from the χ_ν^2 distribution with $\nu = N - 1$.)

Previous analyses of halo models used methods that correspond to finding a $P = 0.68$ confidence region for μ by reporting a region bounded by values of μ such that $\chi^2(\mu) = \chi_{\text{GOF},P}^2$, rather than $\chi^2(\mu) = \chi_{\min}^2 + 1$. One problem with such a procedure is immediately apparent: for nearly a third of all data sets, no such "confidence region" will exist because for 32% of all Gaussian data, $\chi_{\min}^2$ will be greater than the critical value. In fact, for every data set, there will be some constant, C, such that no "confidence region" exists for any confidence level less than C. For those data sets for which such a "confidence region" exists, it will vary in size, sometimes being larger than the correct region, and sometimes smaller.

One might hope that there might be some relationship between the regions such that, on the average, they might coincide. To see that this hope is forlorn, consider a specific, simple problem whose solution is obvious. The simple problem we will discuss is inference of some quantity of unknown magnitude, μ, from data consisting of N measurements of μ, each contaminated with added noise. We will denote the measured values by x_i, and model them as being the sum of μ and noise components to which we assign independent Gaussian probabilities with zero mean and known, common standard deviation, σ. For this problem, both a frequentist analysis and a Bayesian analysis with a broad prior lead to a best estimate of $\mu = \bar x$ and a 68% confidence or credible region of $\bar x \pm \sigma/\sqrt{N}$, where $\bar x$ is the sample mean. We can connect this problem to the above discussion by examining the likelihood, which is simply the product of N Gaussian distributions,

$$\mathcal{L}(\mu) = \frac{1}{\sigma^N (2\pi)^{N/2}} \exp\left[-\frac{\sum (x_i - \mu)^2}{2\sigma^2} \right]. \tag{A2}$$

Its implications for μ can be more clearly seen by expanding the square in the exponential and then completing the square in μ, which gives,

$$\mathcal{L}(\mu) = \frac{1}{\sigma^N (2\pi)^{N/2}} \exp\left[-\frac{Ns^2}{2\sigma^2} \right] \exp\left[-\frac{N(\bar x - \mu)^2}{2\sigma^2} \right], \tag{A3}$$

where $s^2 \equiv \sum(x_i - \bar{x})^2/N$ is the sample variance. As a function of μ, this is proportional to a Gaussian centered at $\bar{x}$ with a width of $\sigma/\sqrt{N}$. Its relationship to the χ^2 procedure just described is obvious once we note that, up to a term constant in μ, the log likelihood is proportional to χ^2:

$$-2\log\mathcal{L}(\mu) \;\; = \;\; \sum\frac{(x_i - \mu)^2}{\sigma^2} + C \qquad\qquad (A4)$$

$$= \;\; \chi^2 + C. \qquad\qquad (A5)$$

Using these results, it is easy to verify that the $\chi^2_{\min} + 1$ interval is exactly the familiar $\bar{x} \pm \sigma/\sqrt{N}$ interval. More importantly, for this simple example we can examine the behavior of the incorrect procedure, where the "confidence region" is bounded by the 68% critical χ^2 value. The half-width of the incorrect region can be found analytically; it is given by

$$\delta = \frac{\sigma}{\sqrt{N}}\left[\chi^2_{68} - \chi^2_{\min}\right]^{1/2}. \qquad\qquad (A6)$$

A good estimate of the average behavior of the region can be found by substituting the expected value of $\chi^2_{\min}$ (equal to $N-1$) and an asymptotic expression for χ^2_{68} (equal to $N + 0.47\sqrt{2N}$), giving

$$\langle\delta\rangle \approx \frac{\sigma}{\sqrt{N}}\left[1 + 0.47\sqrt{2N}\right]^{1/2} \qquad\qquad (A7)$$

(we have verified the accuracy of this expression with Monte Carlo simulations). This gives $\langle\delta\rangle \approx 1.8\sigma/\sqrt{N}$ for $N = 10$, and $\langle\delta\rangle \approx 2.8\sigma/\sqrt{N}$ for $N = 100$. It is thus clear that, on the average, the region will be significantly too large, and that the discrepancy actually grows with the number of data. Finally, the 68% probability associated with this region is obviously not the covering probability for this procedure, since we know the smaller $\sigma/\sqrt{N}$ region has this covering probability. These results clearly show that the use of GOF procedures to find "confidence regions," however intuitively appealing it may at first seem, is incorrect.

It is interesting to speculate about why such a basic mistake is so frequently made. One reason is that, for the familiar case of Gaussian statistics, the same function—χ^2—is used both to define the point-valued statistic used in a GOF test ($\chi^2_{\min}$ or $\chi^2(\mu_0)$), and the interval-valued statistic used for a confidence region (the μ range with $\chi^2 < \chi^2_{\min} + \Delta\chi^2$). This may have been why some investigators used the KS GOF statistic to constrain parameters, although we know of no statistical literature suggesting that this statistic is useful for estimation problems. More fundamentally, the confusion may arise because there are several qualitatively different probabilities in frequentist statistics. Covering probabilities for confidence regions, Type I error probabilities, Type II error probabilities—all of these are quantities that span $[0, 1]$ that scientists can use to assess the reasonableness of hypotheses. But none of them are probabilities *for hypotheses*, so one may easily be confused about which is most closely related to the question one is asking. This confusion is exacerbated by the fact that all frequentist probabilities must condition on a particular point hypothesis, even those that refer to an entire class of hypotheses. For some problems (particularly for confidence region calculations), the hope is that the final result

is independent of the particular hypothesis used. But this is seldom true in real problems, so that one hypothesis must inevitably be chosen to represent a class of hypotheses (e.g., approximate confidence regions are found using calculations conditioning on the best-fit hypothesis).

This confusion cannot arise in the Bayesian approach. One always calculates probabilities for hypotheses, so there is never ambiguity over what kind of hypothesis one's probability is associated with: one must explicitly state it in order even to start the calculation. If one seeks a measure of how plausible it is for a parameter to lie in some region, one simply calculates the probability that it is in that region (parameter estimation). If instead one wishes to assess an entire model, one calculates the probability for that model as a whole (model comparison). The formalism forces one to distinguish between these options.

B. Properties of Halo Models With Luminosity Functions

In this Appendix we derive the properties of the differential burst rate for a halo population with a power-law luminosity function mentioned in § 2. We focus on the slope of the intensity distribution. Consider, therefore, the differential burst rate along a particular line of site, $\mathbf{n}$. Let r denote the distance from the observer along the line of site, and write the burst rate density as $\dot{n}(r, \Lambda) = \dot{n}(r) f(\Lambda)$, where $f(\Lambda)$ is the normalized luminosity function. Then the differential rate is given by

$$\frac{dR}{d\Phi d\mathbf{n}} = \int dr\, r^2 \dot{n}(r) \int d\Lambda\, f(\Lambda) \delta\left(\Phi - \frac{\Lambda}{4\pi r^2}\right). \tag{B1}$$

Changing variables in the δ-function from Φ to r and integrating over r gives

$$\frac{dR}{d\Phi d\mathbf{n}} = \frac{1}{2\Phi} \int d\Lambda\, f(\Lambda) \int dr\, r^3 \dot{n}(r) \delta\left[r - \left(\frac{\Lambda}{4\pi\Phi}\right)^{1/2}\right] \tag{B2}$$

$$= \frac{\Phi^{-5/2}}{16\pi^{1/2}} \int d\Lambda\, \Lambda^{3/2} f(\Lambda)\, \dot{n}\left(\sqrt{\frac{\Lambda}{4\pi\Phi}}\right). \tag{B3}$$

As a simplified description of the halo models considered in the body of the paper, let

$$\dot{n}(r) = \begin{cases} \dot{n}_0, & \text{if } r \leq r_c; \\ \dot{n}_0 \left(\frac{r}{r_c}\right)^{-2}, & \text{if } r > r_c. \end{cases} \tag{B4}$$

Then $dR/d\Phi$ is proportional to $\Phi^{-5/2} I(\Phi)$, where

$$I(\Phi) \equiv \int_{\Lambda_l}^{\Lambda_u} d\Lambda\, \Lambda^{3/2-p} \times \begin{cases} 1, & \text{for } \Lambda \leq 4\pi r_c^2 \Phi; \\ \left(\frac{\Lambda}{4\pi r_c^2 \Phi}\right)^{-1}, & \text{for } \Lambda > 4\pi r_c^2 \Phi. \end{cases} \tag{B5}$$

If Φ is such that the upper limit of the integral is less than $4\pi r_c^2 \Phi$, then only the first case of the integrand is relevant and $I(\Phi)$ is simply a constant. Thus so long as $\Phi \geq \Phi_b$, where $\Phi_b = \Lambda_u/4\pi r_c^2$, we find that $dR/d\Phi \propto \Phi^{-5/2}$, the power law expected for observing a homogeneous population.

If, on the other hand, the lower limit is greater than $4\pi r_c^2 \Phi$, only the second case of the integrand is relevant, and $I(\Phi) \propto \Phi^{-1}$. Thus $dR/d\Phi \propto \Phi^{-3/2}$ when $\Phi < \Phi_a$, where $\Phi_a = \Lambda_l/4\pi r_c^2$.

For intermediate values of Φ, the integrand must be broken into separate cases: we first integrate from Λ_l to $4\pi r_c^2 \Phi$, and then from $4\pi r_c^2 \Phi$ to Λ_u. The result is

$$
\begin{aligned}
I(\Phi) \;=\; & \Phi^{5/2-p} \left(4\pi r_c^2\right)^{5/2-p} \\
& \times \left\{ \frac{1}{5/2-p}\left[1 - \left(\frac{\Phi_a}{\Phi}\right)^{5/2-p}\right] + \frac{1}{p-3/2}\left[1 - \left(\frac{\Phi}{\Phi_b}\right)^{p-3/2}\right] \right\}.
\end{aligned}
\tag{B6}
$$

Now consider the behavior of the terms in braces for the case when $3/2 < p < 5/2$, which is the parameter regime most relevant to GRBs. As long as $\Phi \gg \Phi_a$ and $\Phi \ll \Phi_b$, the Φ-dependent terms are negligible, so $I(\Phi) \propto \Phi^{5/2-p}$. This implies that $dR/d\Phi \propto \Phi^{-p}$ in this region; the Φ-dependent terms merely smooth the transitions from the $\Phi^{-3/2}$ behavior at low fluxes, and to the $\Phi^{-5/2}$ behavior at high fluxes. Figure 4 portrays these results.

C.   Dipole Moments of Halo Models

The intrinsic dipole moment of a shell observed at a radius r' from the Sun is

$$
D(r') = \frac{\int_{-1}^{1} d\mu\, (r')^2 \mu \dot{n}'(r',\mu)}{\int_{-1}^{1} d\mu\, (r')^2 \dot{n}'(r',\mu)},
\tag{C1}
$$

where $\dot{n}'(r,\mu)$ is the burst rate per unit volume at a distance r' along any direction that makes an angle $\theta = \cos^{-1}\mu$ with the Galactic center. We presume here a burst rate that is spherically symmetric about the Galactic center, so no azimuthal dependence enters. If the burst rate per unit volume at a Galactocentric distance r is $\dot{n}(r)$, then by the law of cosines

$$
\dot{n}'(r',\mu) = \dot{n}[(r_0^2 + (r')^2 + 2r'r_0\mu)^{1/2}].
\tag{C2}
$$

For the halos we consider above, $\dot{n}(r) \propto 1/(r^2 + r_c^2)$, and the integrals required to evaluate $D(r')$ can be done analytically, giving

$$
D(r') = \frac{1}{2}\left[\rho' + \frac{1}{\rho'} + \frac{\rho_c^2}{\rho'} - \frac{4}{\ln\left(\frac{(\rho'+1)^2 + \rho_c^2}{(\rho'-1)^2 + \rho_c^2}\right)}\right],
\tag{C3}
$$

where $\rho' = r'/r_0$ and $\rho_c = r_c/r_0$. This expression is somewhat complicated, and an amazing amount of cancellation occurs between the various terms. We gain more insight into the behavior of $D(r')$ by approximating it in the limit where r_0 is small compared with the other length scales (r' and r_c). Due to the high-order cancellation among the terms in equation (C3), the approximate result is best found by separately approximating the integrals in equation (C1). The result is

$$
D(r') \approx \frac{2}{3} \frac{1}{\rho' + \frac{1}{\rho'} + \frac{\rho_c}{\rho'}},
\tag{C4}
$$

as cited in the main text. The approximation is surprisingly good for all ranges of the parameters discussed in this work.

REFERENCES

Allen, C. W. 1973, Astrophysical Qunatities (London: Athlone Press)

Atteia, J.-L., et al. 1987, ApJ Supp., 64, 305

Bahcall, J. N., & Soneira, R. M. 1980, ApJ Supp., 44, 73

Band, D. L., et al. 1994, ApJ, 434, 560

Band, D. L., et al. 1995, ApJ, 447, 289

Brainerd, J. J. 1992, Nature, 355, 522

Briggs, M. 1996, in Gamma-Ray Bursts, Huntsville, AL 1995, (New York: AIP) in press

Eadie, W. T., Drijard, D., James, F. E., Roos, M., & Sadoulet, B. 1971, Statistical Methods in Experimental Physics (Amsterdam: North-Holland Publishing Company)

de Vaucouleurs, G., de Vaucoulerus, A., Corwin, H. G., Jr., Buta, R. J., Paturel, G., & Fouqué, P. 1991, Third Reference Catalog of Bright Galaxies (New York: Springer-Verlag)

Fishman et al. 1994, ApJ Supp., 92, 229

Fishman et al. 1996, ApJ Supp., 106, 65

Frail, D. A. 1996, High Velocity Neutron Stars and Gamma-Ray Bursts, ed. R. E. Rothschild & R. E. Lingenfelter (New York: AIP), 3

Freeman, P. E., Lamb, D. Q., Wilson, R. B., Briggs, M., Paciesas, W., Preece, R., & Band, D. 1996, in Gamma-Ray Bursts, Huntsville, AL 1995, (New York: AIP) in press

Golenetskii, S. V. 1988, Adv. Space. Res., 8, 653

Goodman, J. 1986, ApJ, 308, L47

Graziani, C., & Lamb, D. Q. 1996, to appear in Gamma-Ray Bursts, Third Workshop, Huntsville, AL 1995, (New York: AIP)

Hakkila, J., Meegan, C. A., Pendleton, G. N., Fishman, G. J., Wilson, R. B., Paciesas, W. S., Brock, M. N., &Horack, J. M. 1994, ApJ, 422, 659

Hakkila, J., Meegan, C. A., Pendleton, G. N., Horack, J. M., Briggs, M. S., Paciesas, W. S., & Emslie, A. G. 1995, ApJ, 454, 134

Hartmann, D. 1994, Gamma-Ray Bursts, Second Workshop, ed. G. J. Fishman, J. J. Brainerd & K. Hurley (New York: AIP), 562

Hartmann, D., & Epstein, R. I. 1989, ApJ, 346, 960

Hartmann, D., & Blumenthal, G. R. 1989, ApJ, 342, 521

Hartmann, D., Epstein, R. I., & Woosley, S. E. 1990, ApJ, 348, 625

Higdon, J. C., & Lingenfelter, R. E. 1986, ApJ, 307, 197

Higdon, J. C., & Lingenfelter, R. E. 1990, ARAA, 28, 401

Hurley, K. 1986, in Gamma-Ray Bursts, ed. E. P. Liang & V. Petrosian (New York: AIP), 1

Hartmann, D. H., Brown, L. E., The, L.-S., Linder, E. V., Petrosian, V., Blumenthal, G. R., & Hurley, K. C. 1994, ApJS, 90, 893

Jennings, M. C. 1988, ApJ, 333, 700

Katz, J. I., & Canel, L. M. 1996, in Gamma-Ray Bursts, Huntsville, AL 1995, (New York: AIP) in press

Kouveliotou, C., Meegan, C. A., Fishman, G. J., Bhat, N. P., Briggs, M. S., Koshut, T. M., Paciesas, W. S., & Pendleton, G. N. 1993, ApJ, 413, L101

Kouveliotou, C., Koshut, T. M., Briggs, M. S., Pendleton, G. N., Meegan, C. A., Fishman, G. J., & Lestrade, J. P. 1996, in Gamma-Ray Bursts, Huntsville, AL 1995, (New York: AIP) in press

Lamb, D. Q., Graziani, C., & Smith, I. A. 1993, ApJ, 413, L11

Lamb, D. Q., Wasserman, I. M., & Wang, J. C. L. 1990, ApJ, 363, 670

Lamb, D. Q. 1995, PASP, 107, 1152

Liang, E. P., & Petrosian, V. (eds.) 1986, Gamma-Ray Bursts (New York: AIP)

Loredo, T. J., & Wasserman, I. M. 1993, in Compton Gamma-Ray Observatory, St. Louis, MO 1992, ed. M. Friedlander, N. Gehrels & D. J. Macomb (New York: AIP), 749

Loredo, T. J., & Wasserman, I. M. 1995 (LW95), ApJS, 96, 261

Loredo, T. J., & Wasserman, I. M. 1996, submitted to ApJ

Lyne, A. G., & Lorimer, D. R. 1994, Nature, 369, 127

Mazets, E. P., & Golenetskii, S. V. 1987, Astronomia, 32, 16

Meegan, C. A., Fishman, G. J., & Wilson, R. R. 1985, ApJ, 291, 479

Meegan, C. A., Fishman, G. J., Wilson, R. B., Paciesas, W. S., Pendleton, G. N., Horack, J. M., Brock, M. N., & Kouveliotou, C. 1992b, Nature, 355, 143

Paciesas, W., et al. 1996, in Gamma-Ray Bursts, Huntsville, AL 1995, (New York: AIP) in press

Paczyński, B. 1986, ApJ, 308, L43

Paczyński, B. 1990, ApJ, 348, 485

Paczyński, B. 1995, PASP, 107, 1167

Paczynski, B., & Long, K. 1988, ApJ, 333, 694

Palmer, D. M., et al. 1994, ApJ, 433, L77

Pendleton, G. et al. 1996, to appear in Gamma-Ray Bursts, Third Workshop, Huntsville, AL 1995, (New York: AIP)

Reid, M. J. 1993, ARAA, 31, 345

Rothschild, R. E. 1996, High Velocity Neutron Stars and Gamma-Ray Bursts, ed. R. E. Rothschild & R. E. Lingenfelter (New York: AIP), 51

Schmidt, M., Higdon, J. C., & Hueter, G. 1988, ApJ, 329, L85

Usov, V. V., & Chibisov, G. V. 1975, Sov. Astr., 19, 115

van den Bergh, S. 1983, Ap. Space Sci., 97, 385

Wang, J. C. L., et al. 1989, Phys. Rev. Lett., 63, 1550

Wang, V. C. 1996, to appear in Gamma-Ray Bursts, Third Workshop, Huntsville, AL 1995, (New York: AIP) in press

Wilson, J. R., & Mathews, G. J. 1995, Phys. Rev. Let., 75, 4161

Yamagami, T., & Nishimura, J. 1986, Apl. Sp. Sci., 121, 241

Fig. 1.— Credible regions for the dimensionless luminosity, ν_h, and dimensionless core size, ρ_c, of a halo model, based on the 64 ms (a) and 1024 ms (b) data. Throughout this work crosses show the best-fit parameter values; contours bound the 68.3% (dotted), 95.4% (dashed), and 99.7% (solid) credible regions of highest posterior density.

Fig. 2.— As in Fig. 1, but for models omitting the halo around M31.

Fig. 3.— As in Fig. 1, but for models using a $1/(1 + r/r_c)$ halo. Only results from the 1024 ms data are shown.

Fig. 4.— Joint credible regions for the burst rate density $\dot{n}_0$ and luminosity parameter ν_h, conditional on the best-fit values of the core size for each data set (a), and on a common value of $\rho_c = 10$ (b).

Fig. 5.— Schematic behavior of the differential burst rate for a halo with a bounded power law luminosity function proportional to Λ^{-p}.

Fig. 6.— Log-likelihood vs. dimensionless upper luminosity ν_u for models with a $\Lambda^{-1.8}$ luminosity function with a dynamic range of 10^3. Results are shown for both the 64 ms (solid) and 1024 ms (dashed) data. (a)— Results with ρ_c fixed to the best-fit standard candle model values ($\rho_c = 18.1$ for 64 ms, 7.8 for 1024 ms). (b)—Results with ρ_c slightly reduced (to 10 for the 64 ms data, and 5 for the 1024 ms data).

Fig. 7.— Visibility of large Galactocentric shells. Only the highlighted part of a Galactocentric shell of radius r is visible, if r is comparable to the maximum solarcentric radius, r', from which bursts are visible. The visible portion has a large negative dipole moment.

Fig. 8.— Burst rate per unit radius, and dipole moment of solarcentric shells of radius r' for standard candle models (a, b) and models with a broad luminosity function (c, d).

Fig. 9.— Dipole moments of the models of Figure 8, versus peak flux rather than radius. Points with error bars denote the measured dipole moments of 5 subsets of the data in bins of equal logarithmic width.

Fig. 10.— Profile likelihood vs. the dimensionless luminosity ν_h of the halo component of two-population models, for 64 ms (solid) and 1024 ms (dashed) data.

Fig. 11.— Joint credible regions for f and ν_c for two-population models with luminous halo bursters, based on the 64 ms (a) and 1024 ms (b) data.

Fig. 12.— Predicted (smooth curve) and observed (histogram) cumulative intensity distributions of best-fit two-population models with luminous halo bursters, for 64 ms (a) and 1024 ms (b) data.

Fig. 13.— Differential rates for the halo (dashed) and cosmological (dotted) components comprising the models of Figure 12. The solid curve shows the total differential rate.

Fig. 14.— As Fig. 11, but for models with dim halo bursters.

Fig. 15.— As Fig. 12, but for models with dim halo bursters.

Fig. 16.— Differential rates for the halo (dashed) and cosmological (dotted) components comprising the models of Figure 12. The solid curve shows the total differential rate.

Fig. 17.— Credible regions for f and ν_c for two-population models whose halo component has an intermediate luminosity ($\nu_h = 1.5$, corresponding to the middle mode in Fig. 10), base on 1024 ms data.

Fig. 18.— The predicted peak flux distribution for the best-fit $\nu_h = 1.5$ two-population model for the 1024 ms data. (a) Predicted (smooth curve) and observed (histogram) cumulative intensity distributions. (b) Total differential rate (solid), with halo (dashed) and cosmological (dotted) components plotted separately.

Table 1.   Standard Candle Halo Models

Quantity	64 ms Results	1024 ms Results
ρ_c	18.1	7.8
ν_h	2.20×10^3	3.50×10^2
$\dot{n}_0$ (yr^{-1} kpc^{-3})	4.2×10^{-6}	3.7×10^{-5}
$R_{9,4}$	1.11	5.05
$p(> R_{9,4})$	$\cdots$	$\cdots$
$B_{9,4}$	0.062	0.49

Table 2.   Two-Component Models

Quantity	64 ms Results	1024 ms Results
M_{11}: Luminous Halo Sources		
ν_c	0.16	0.37
ν_h	34.3	19.1
f	0.11	0.073
$R_{11,4}$	3.19	2.14
$p(> R_{11,4})$	0.31	0.47
$B_{11,4}$	0.45	0.25
M_{12}: Dim Halo Sources		
ν_c	3.82	1.38
ν_h	$\equiv 0.01$	0.01
f	0.59	0.36
$R_{12,4}$	8.25	46.1
$p(> R_{12,4})$	0.12	0.022
$B_{12,4}$	2.5	6.7
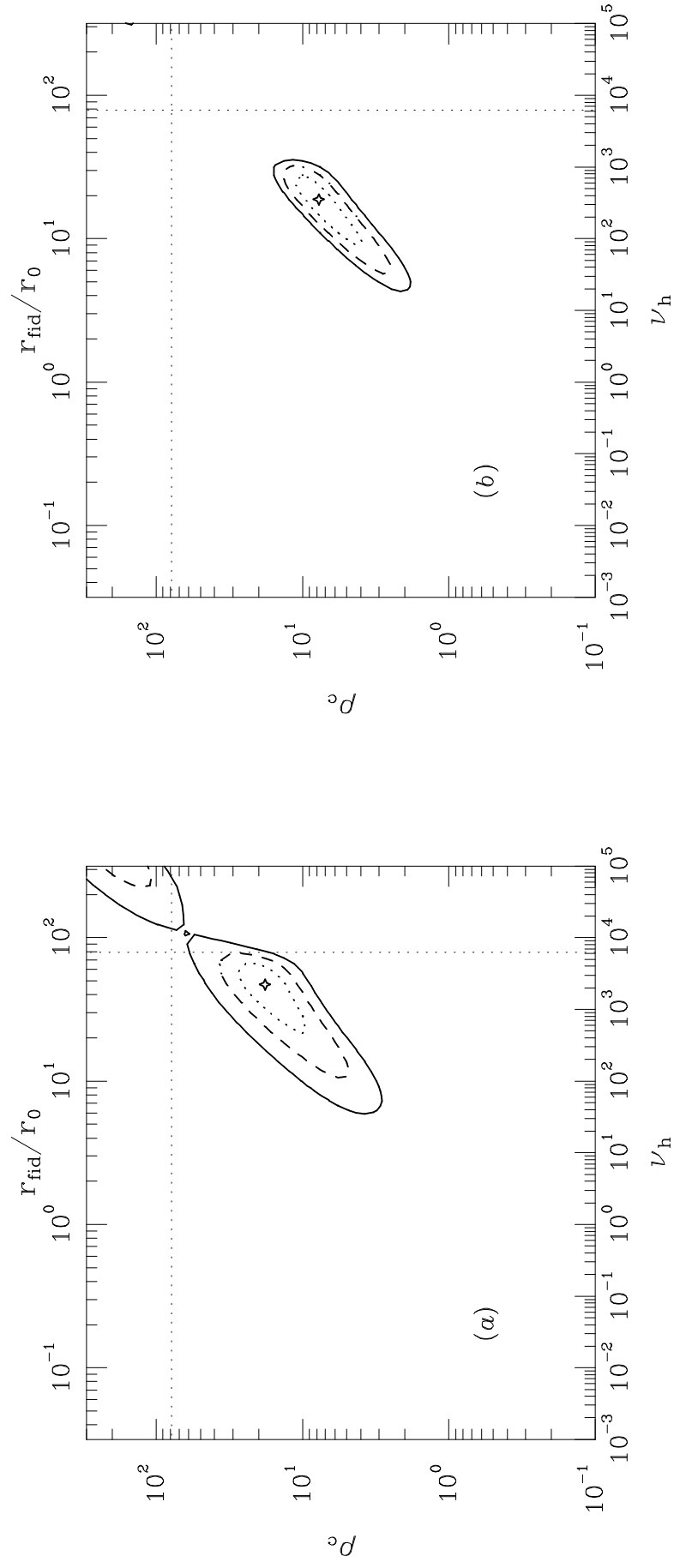
Figure 1

Figure 2

Figure 3

(a)

64 ms

1024 ms

ν_h

$n_0 \ (yr^{-1} \ kpc^{-3})$

Figure 4a

(b)

64 ms

1024 ms

ν_h

n_0 (yr^{-1} kpc^{-3})
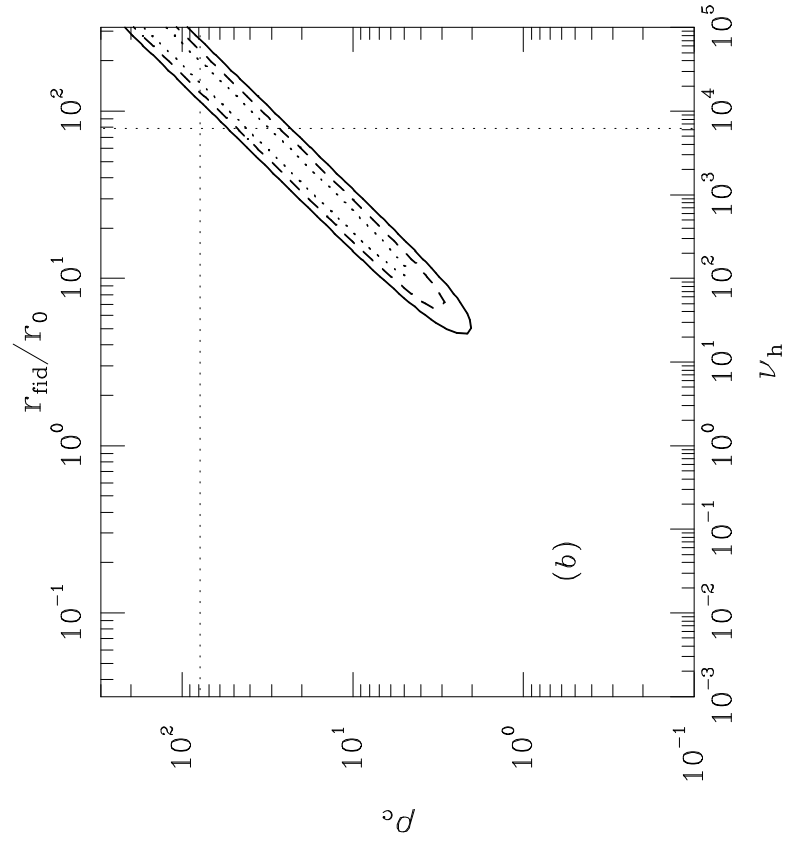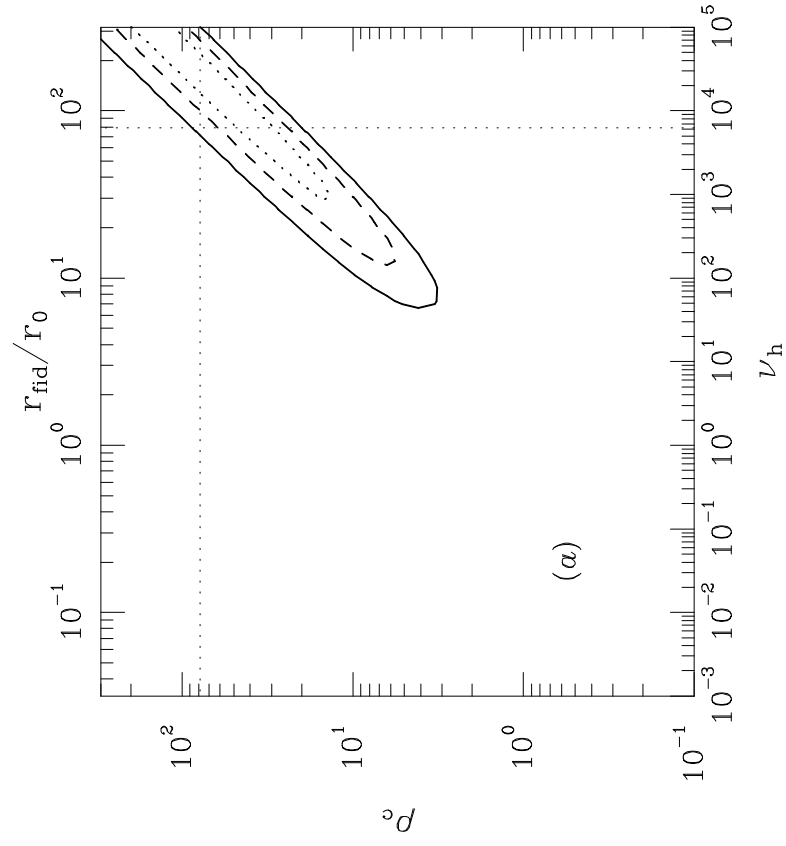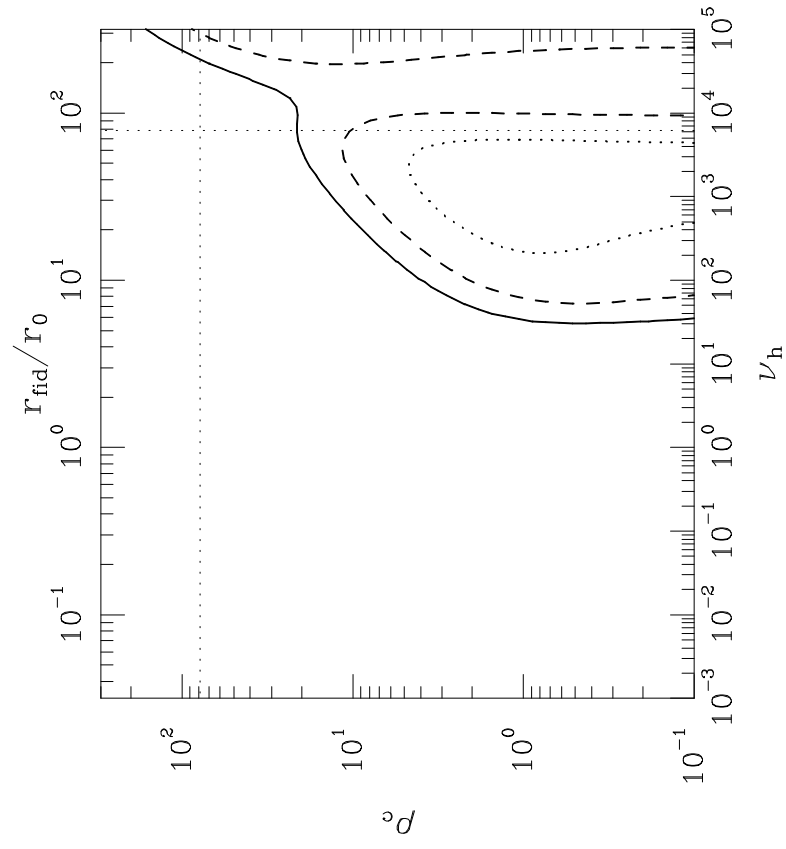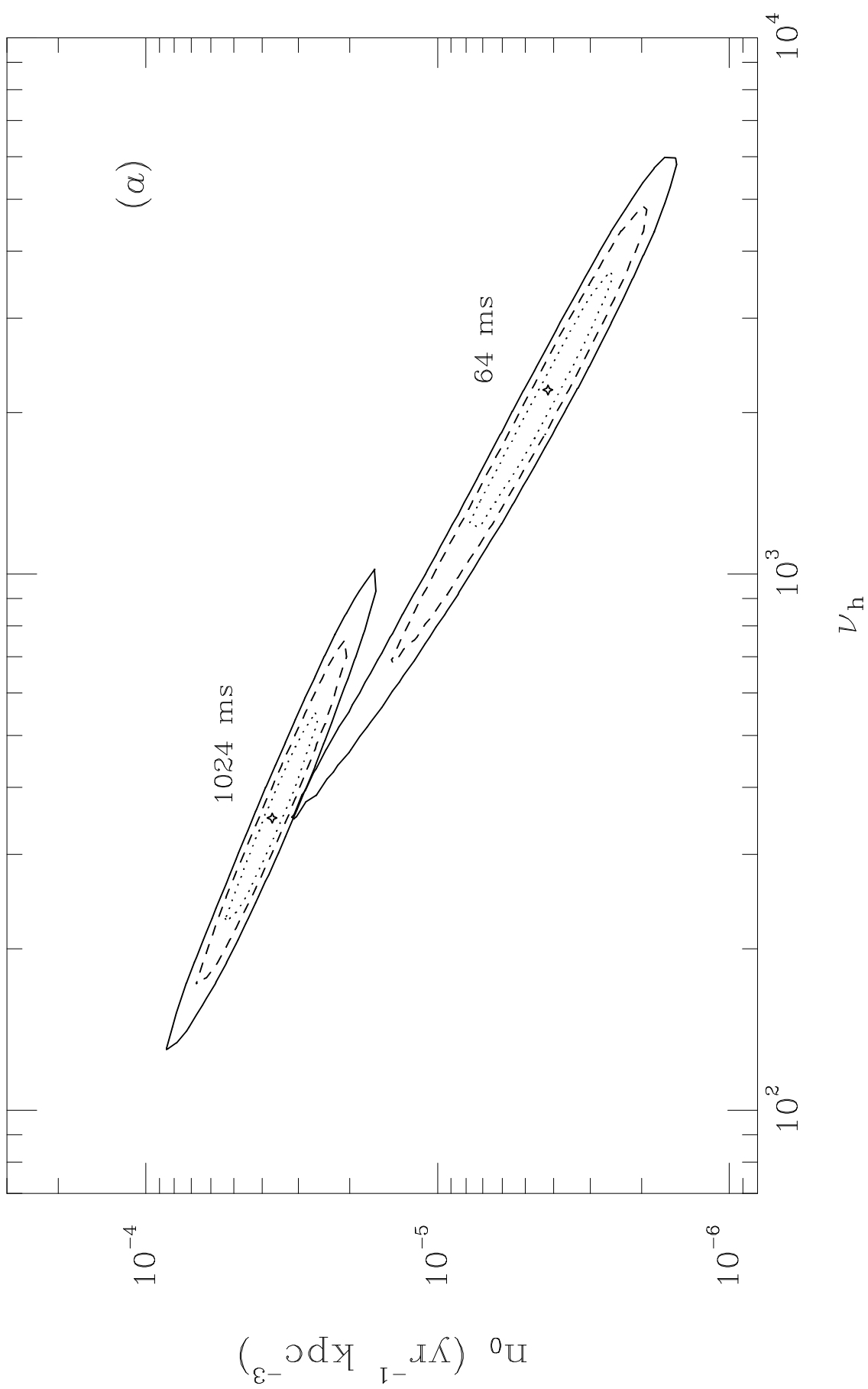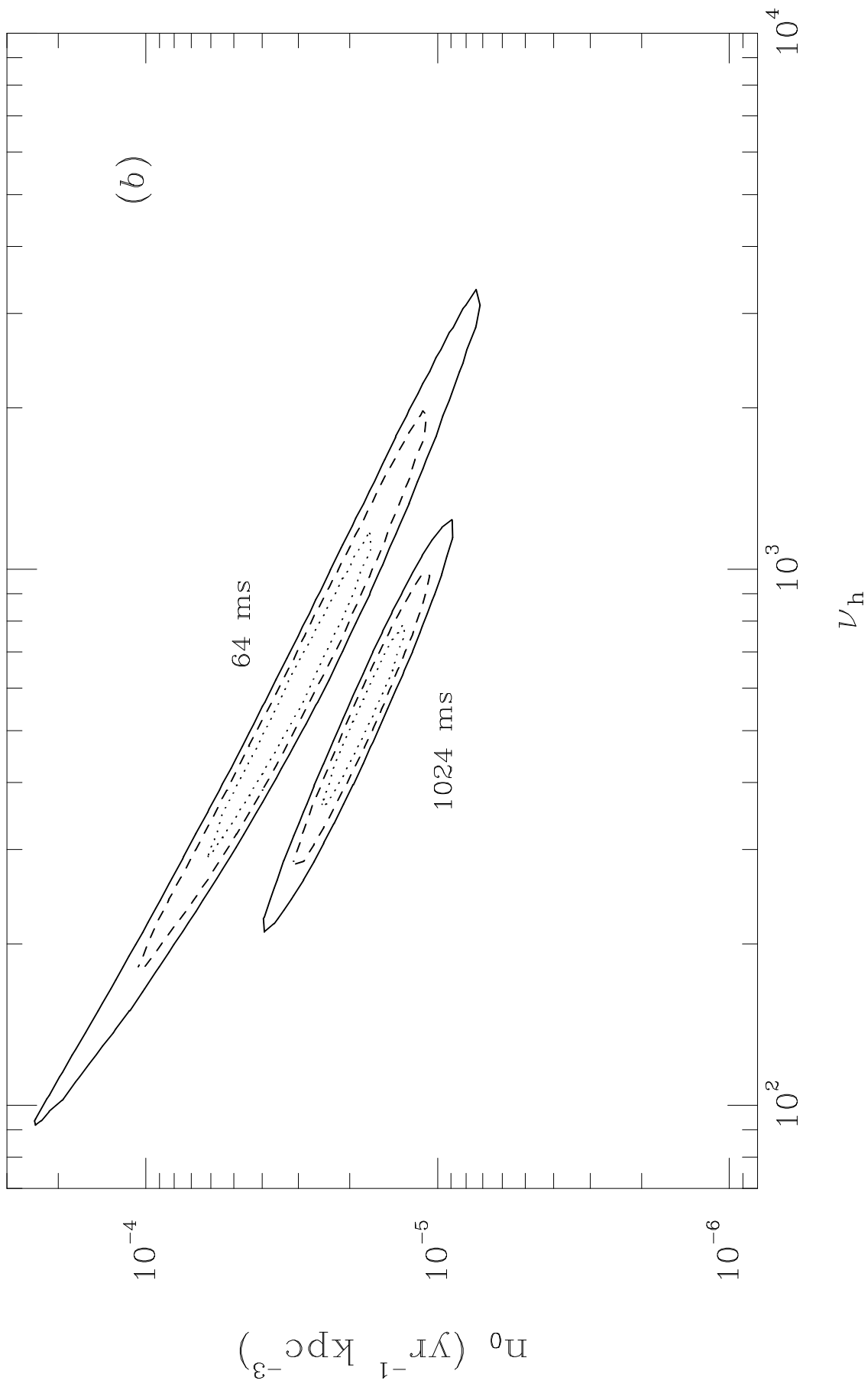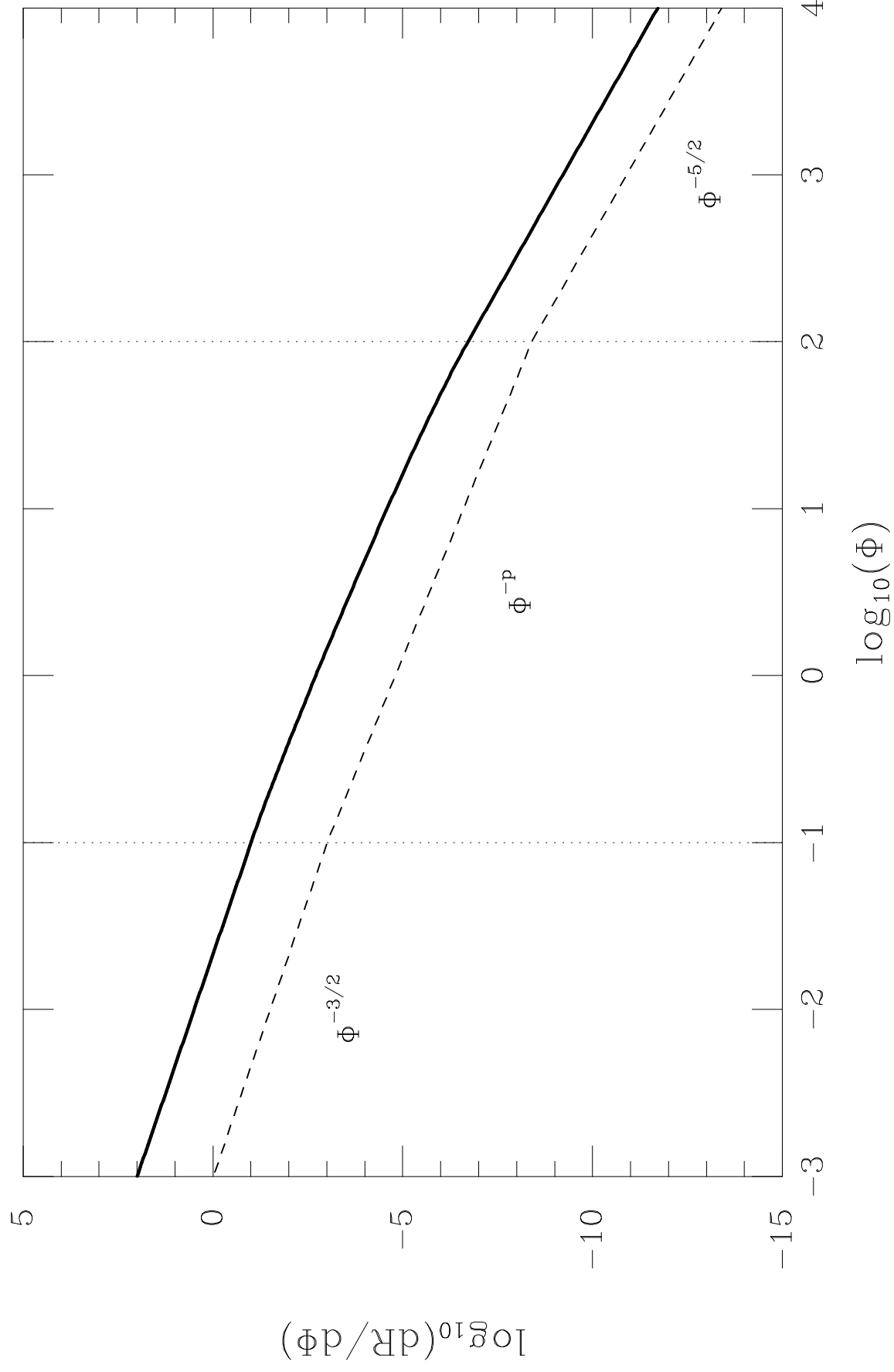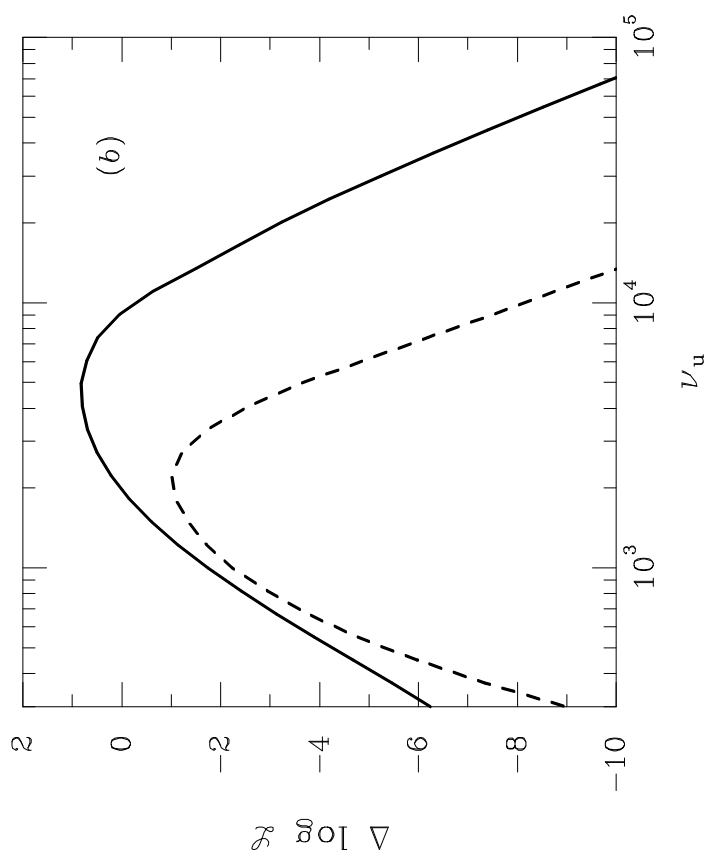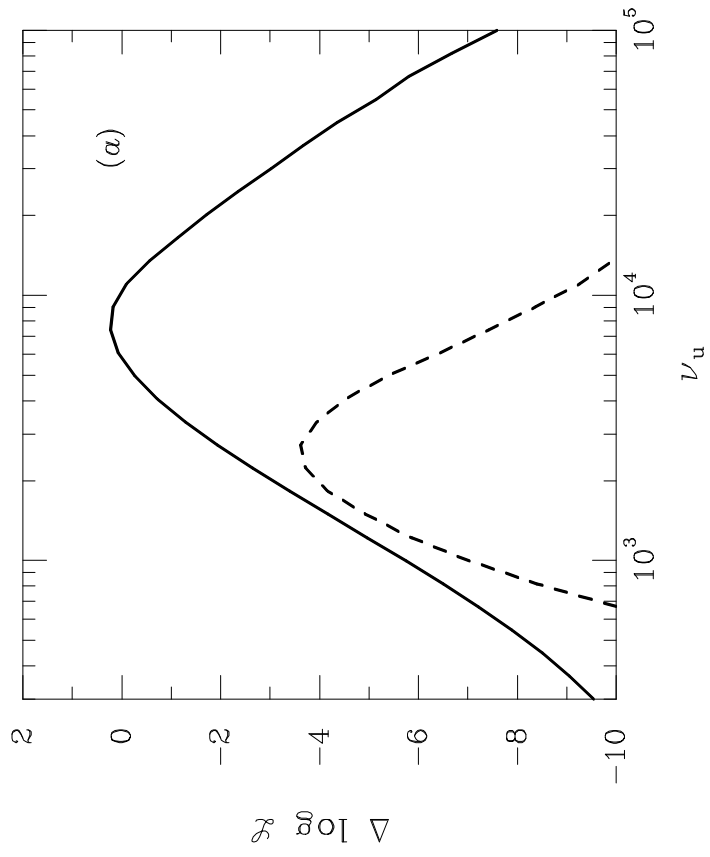
Figure 4b

Figure 5
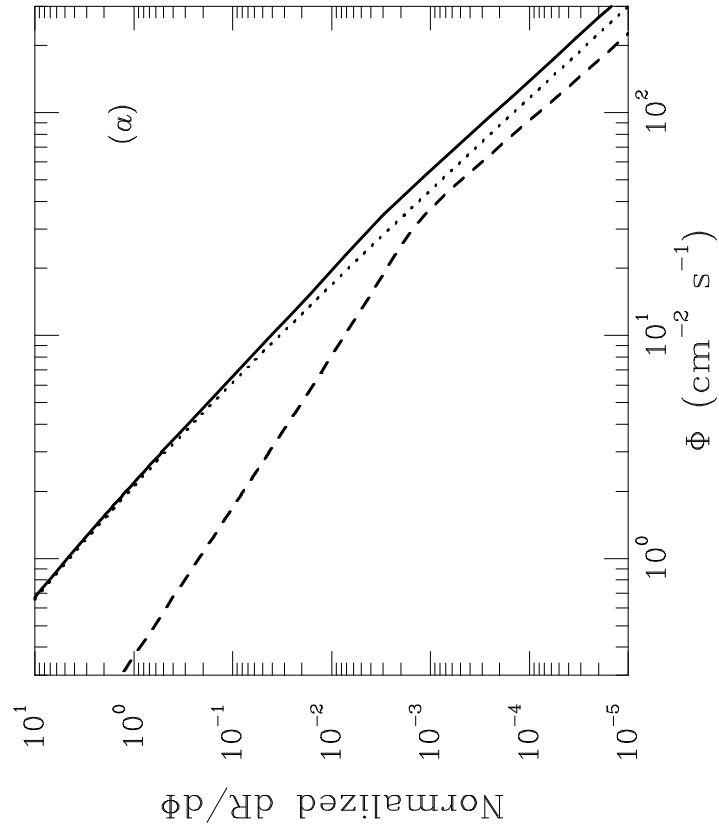
Figure 6
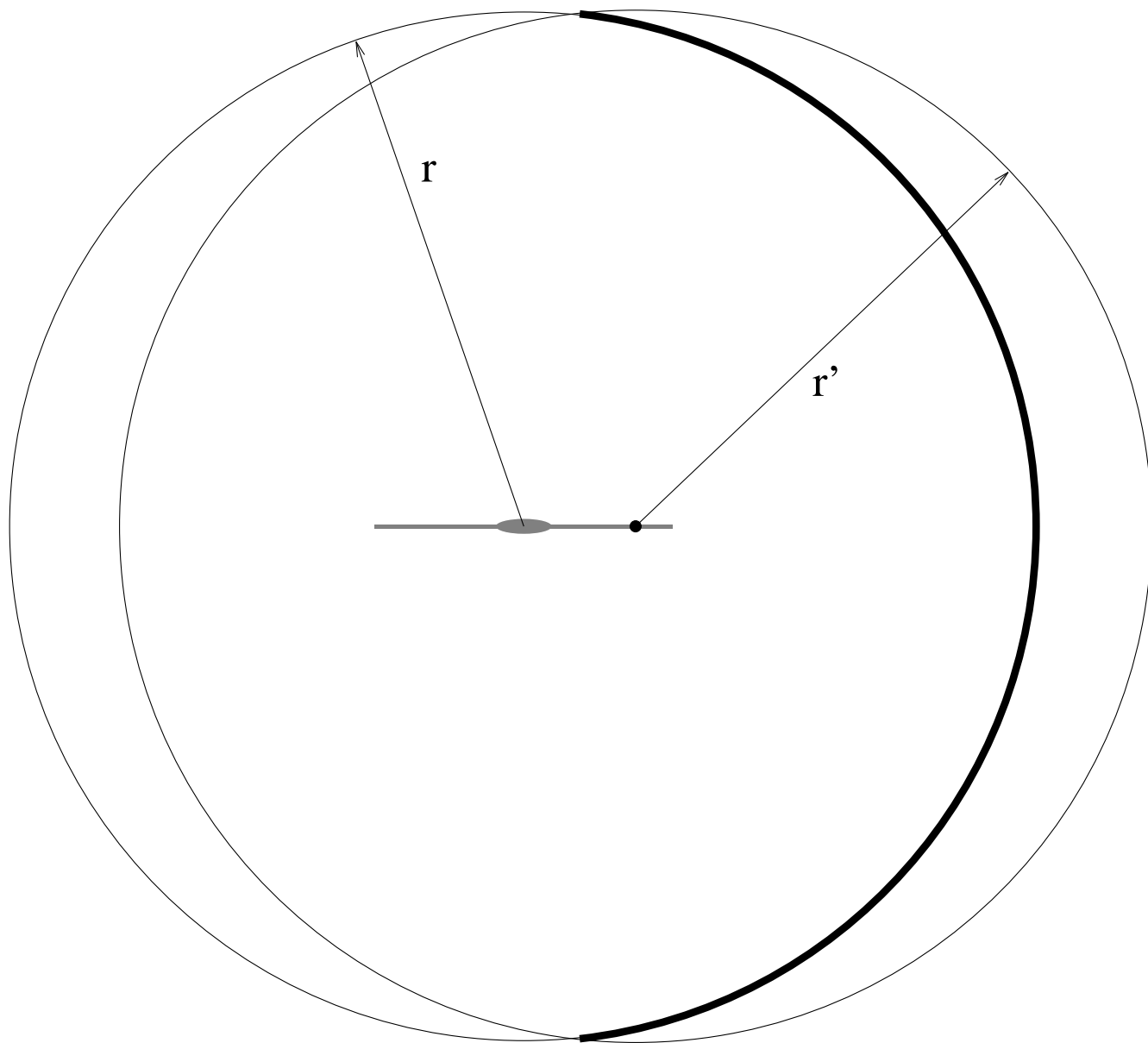
Figure 7
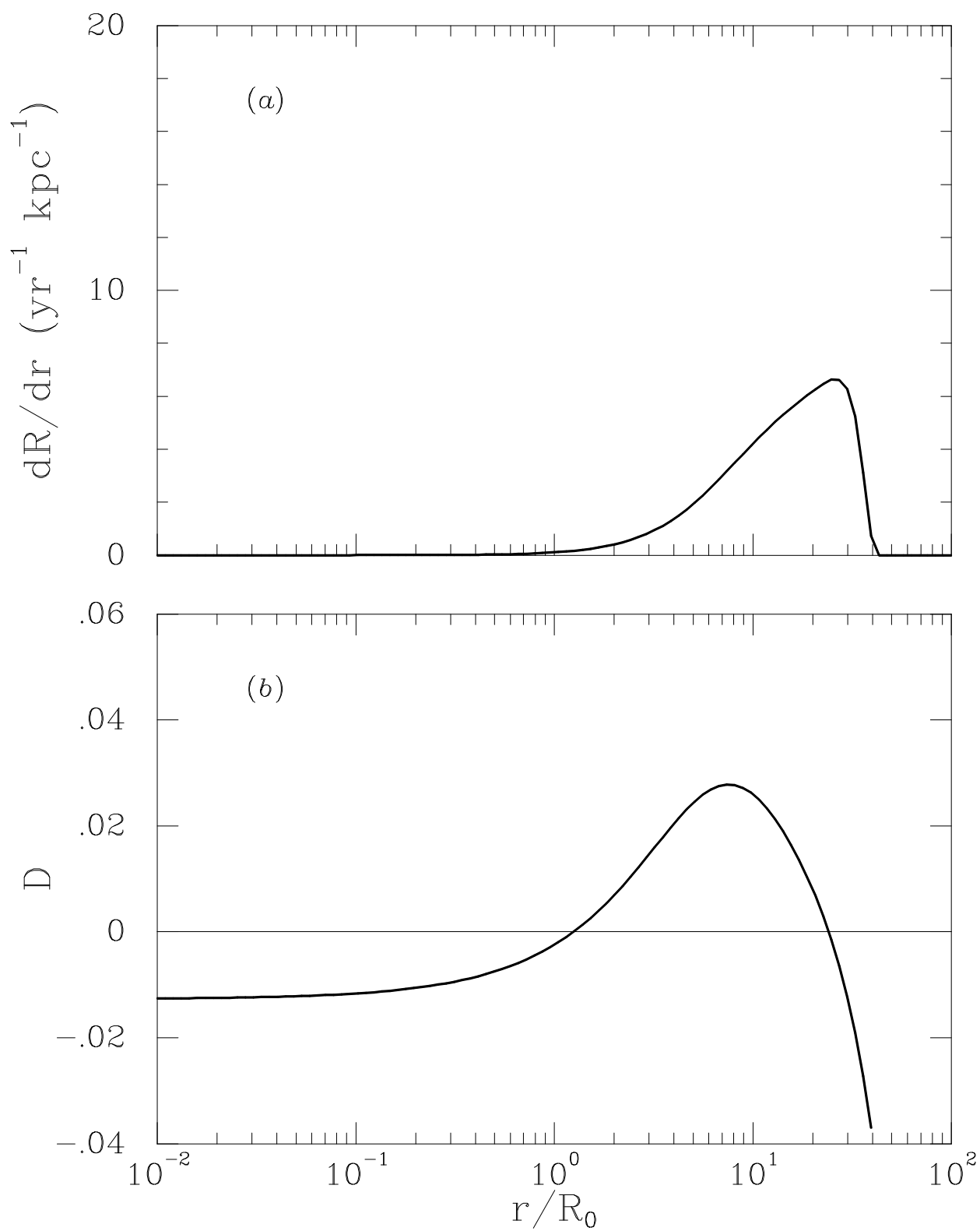
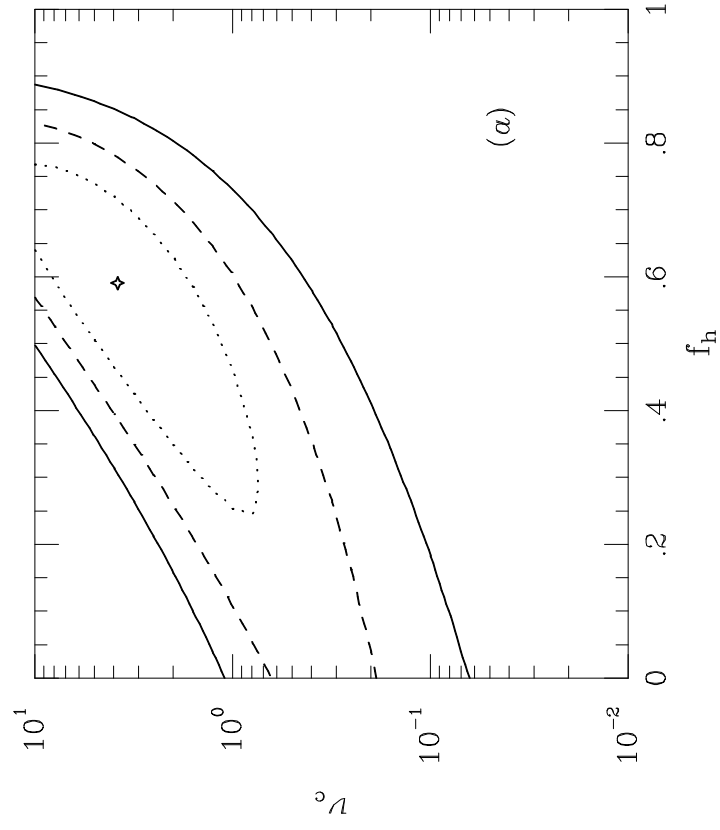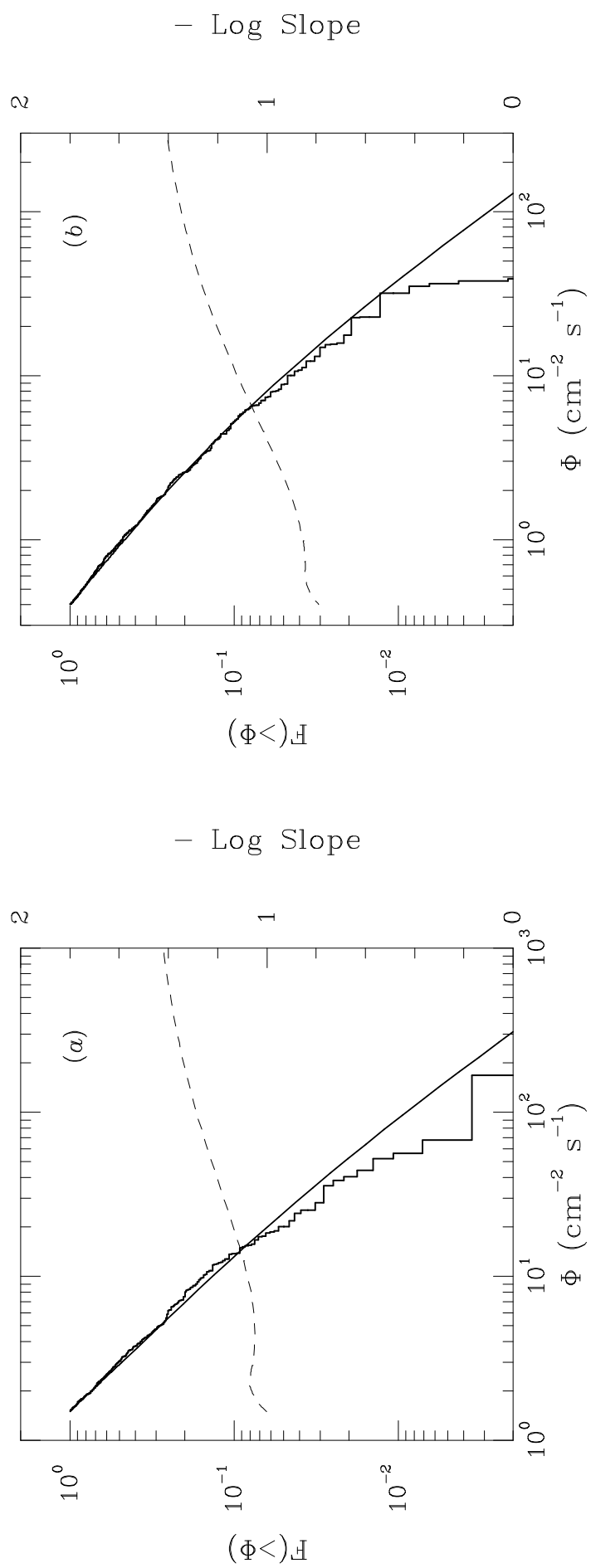Figure 8 (a, b)
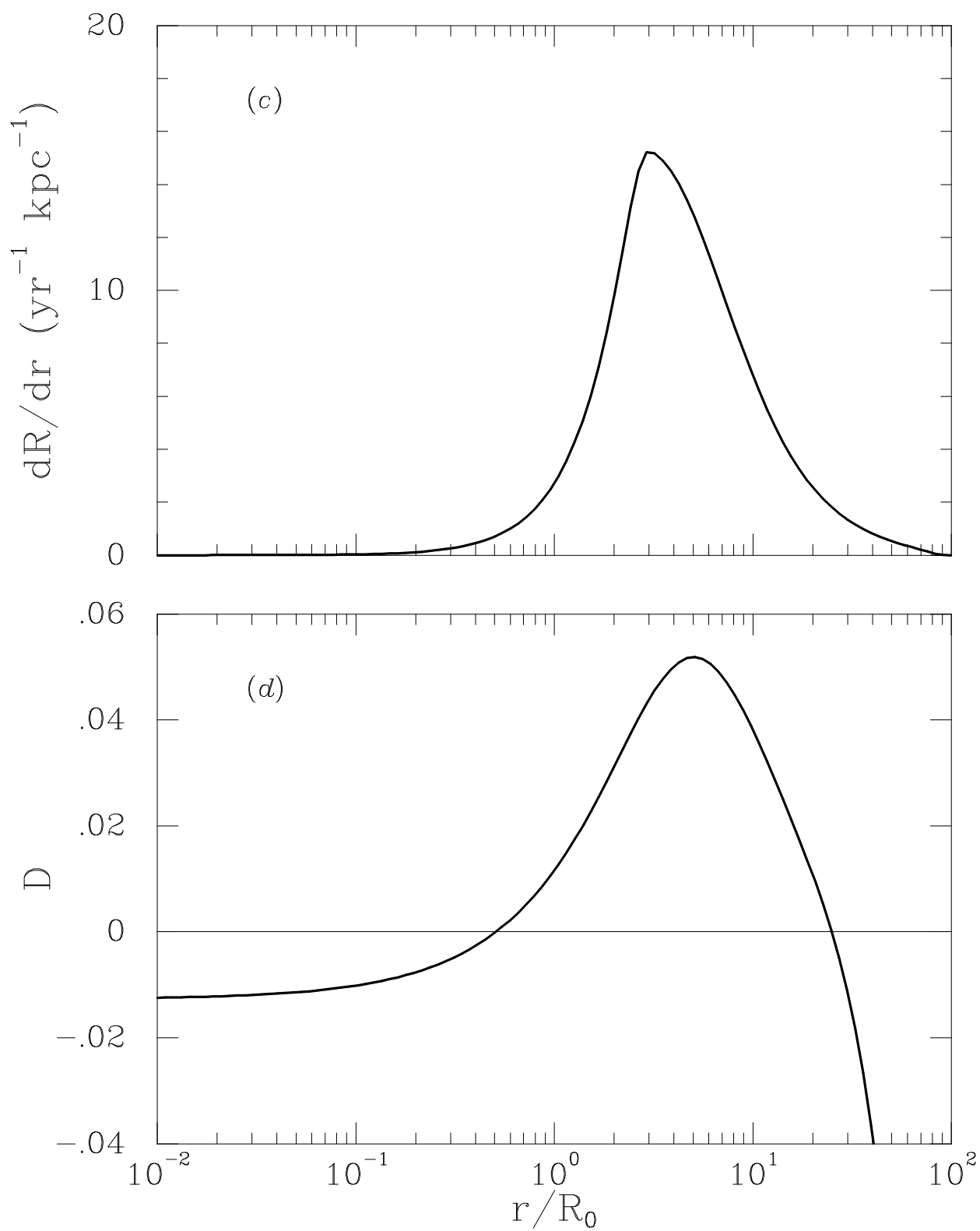
Figure 8 (c, d)
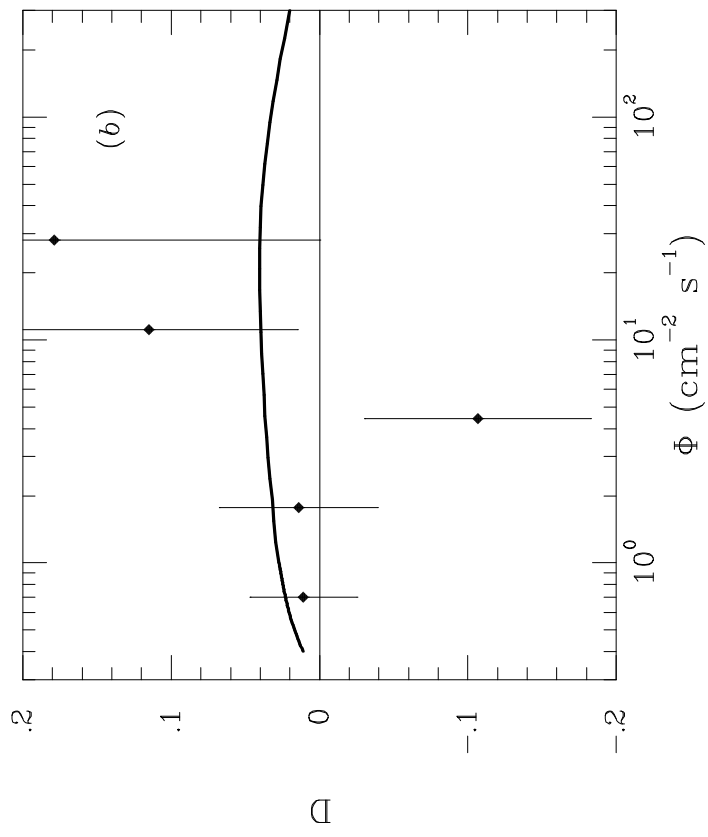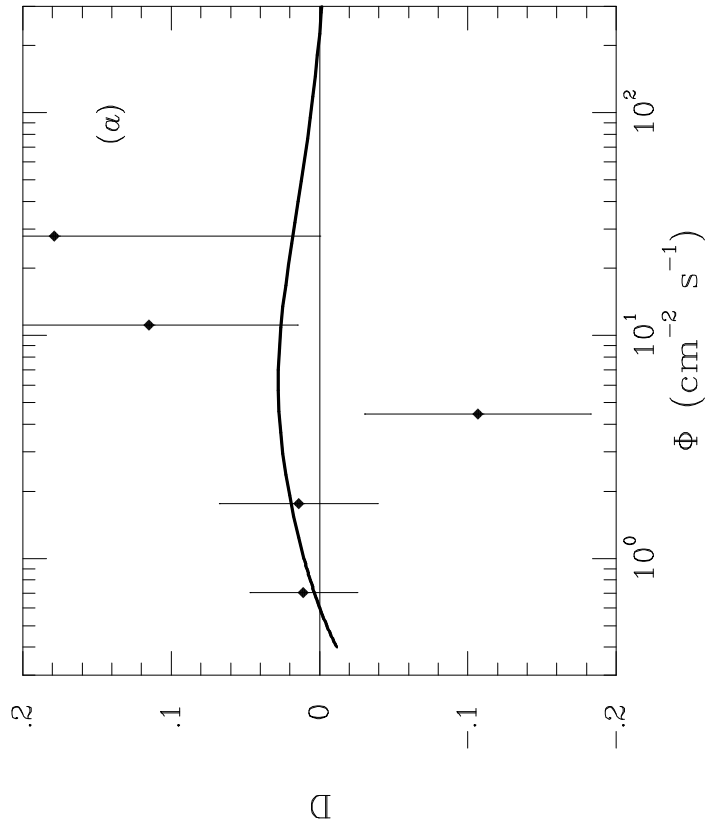
Figure 9
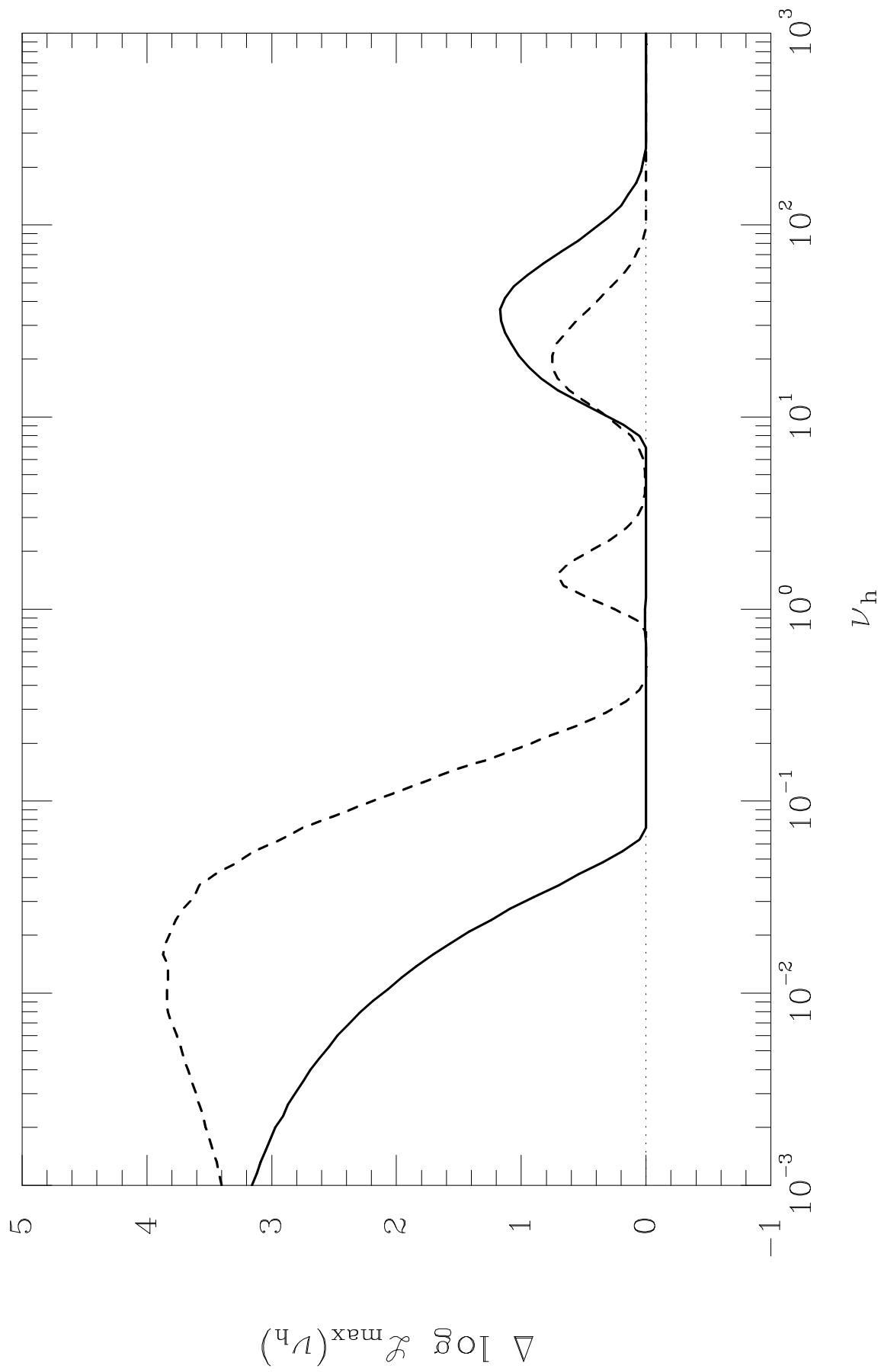
Figure 10
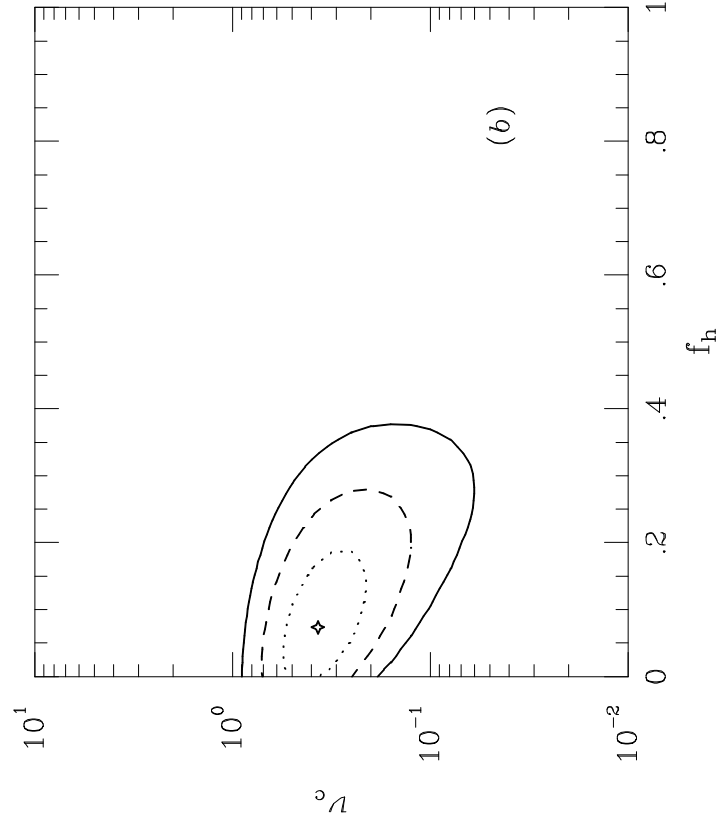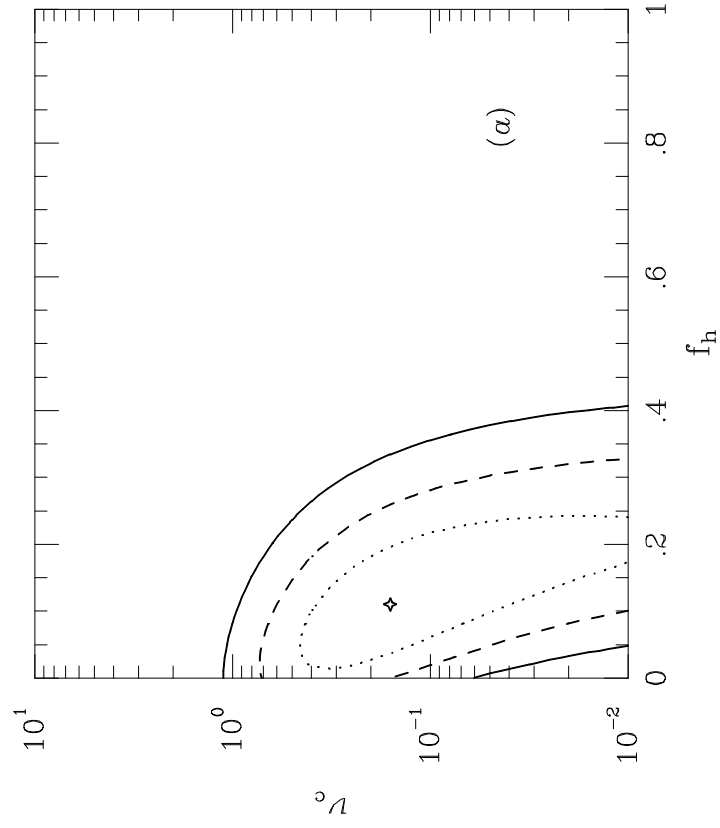
Figure 11
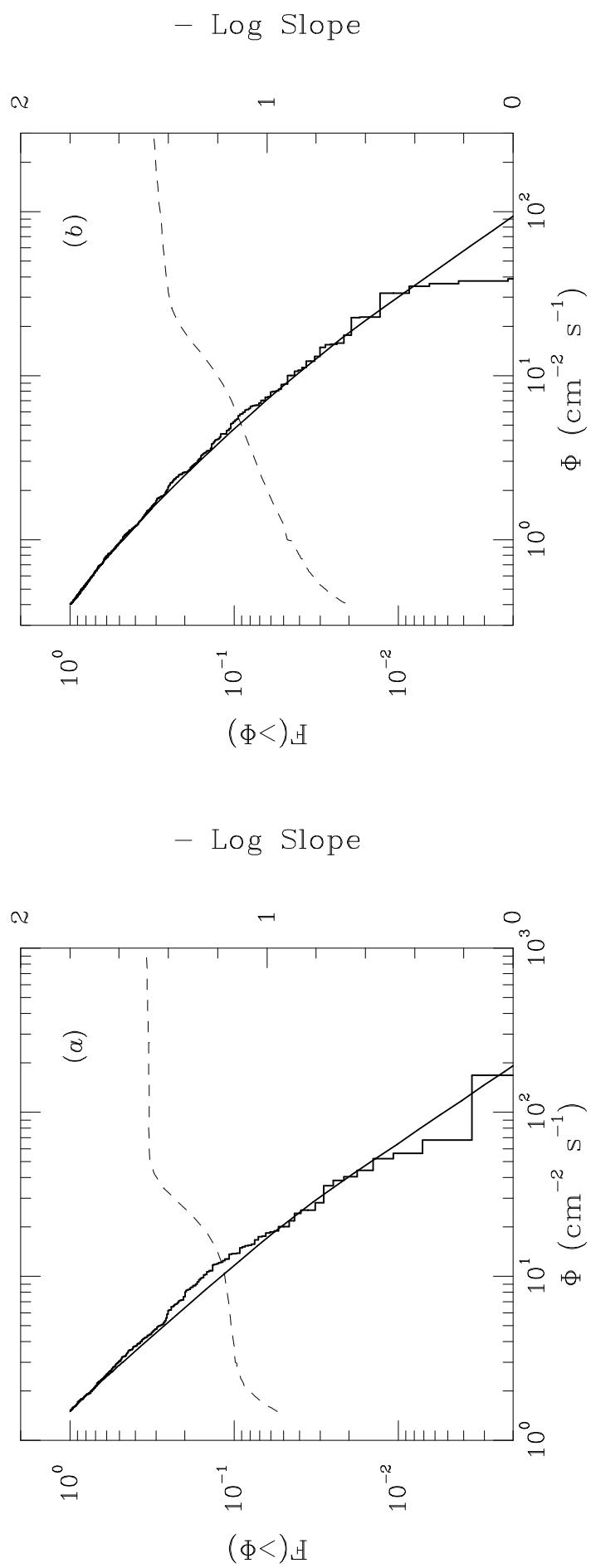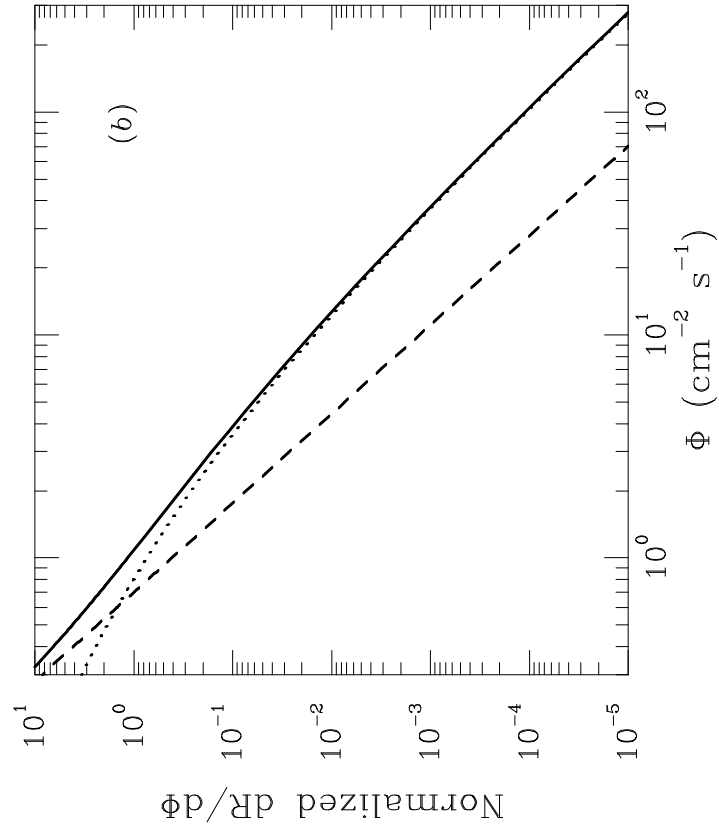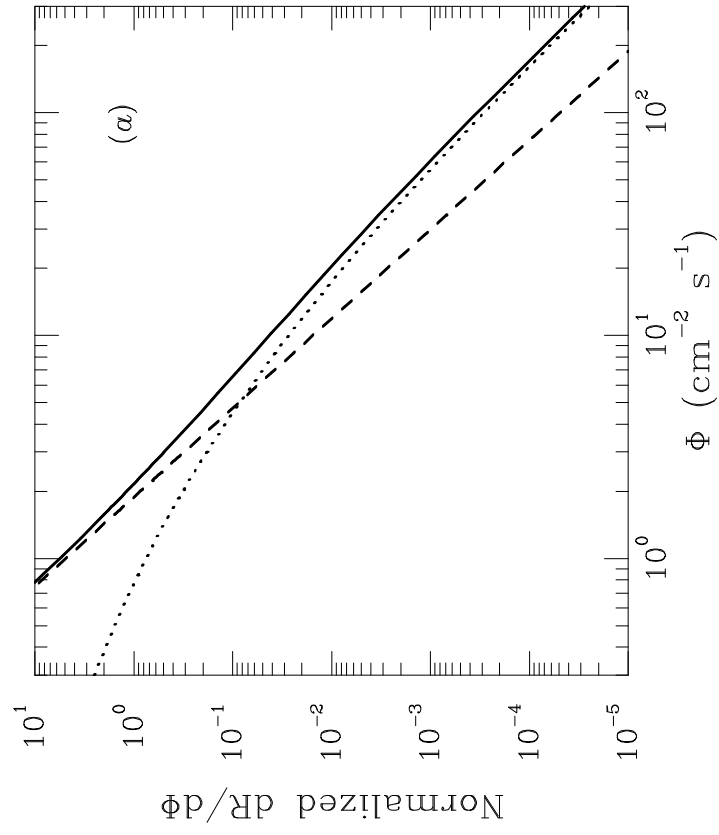
Figure 12
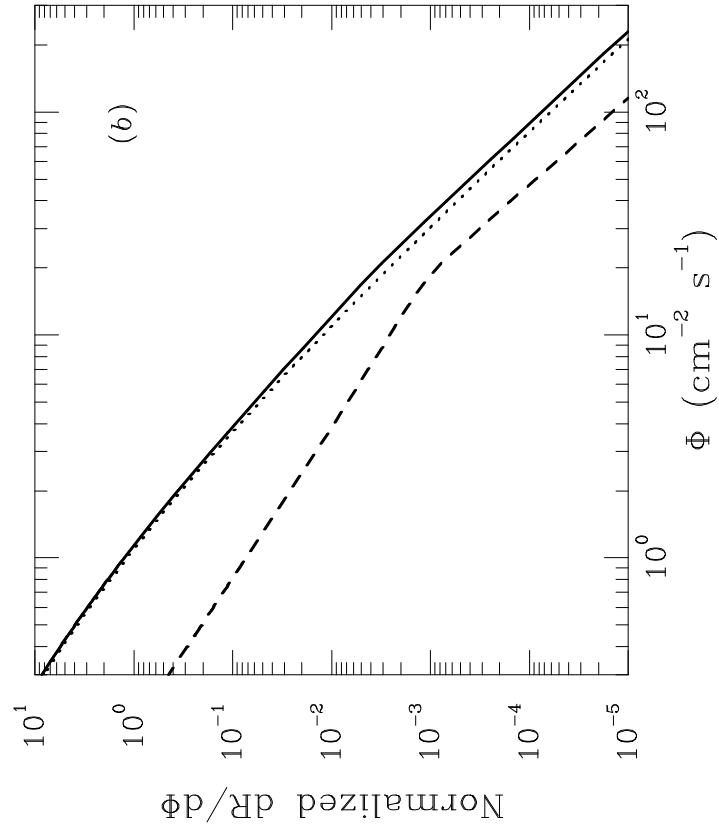
Figure 13
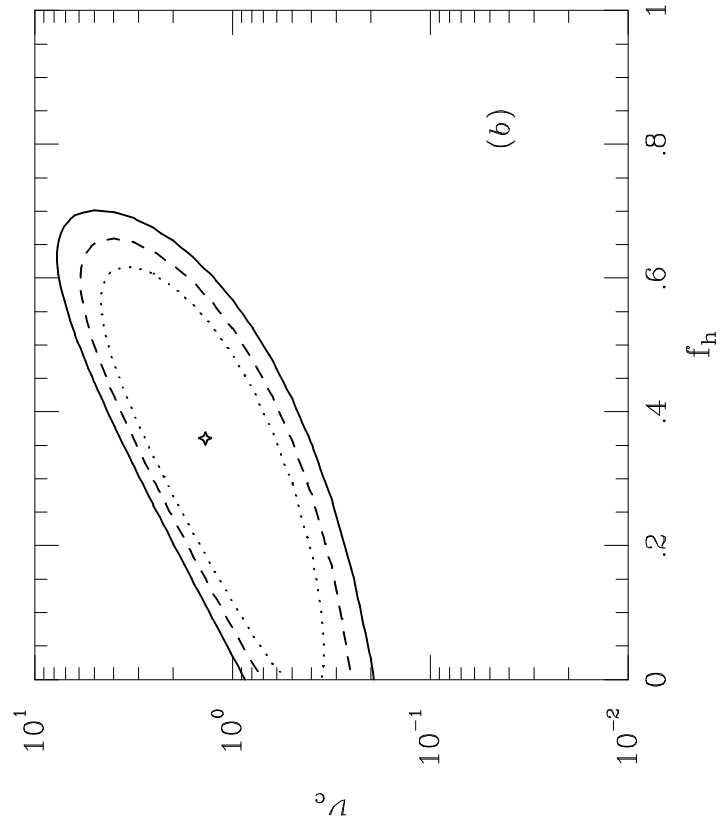
Figure 14

Figure 15

Figure 16

Figure 17

$\Phi \ (\mathrm{cm^{-2} \ s^{-1}})$

$-$ Log Slope

Normalized $dR/d\Phi$

$\Phi \ (\mathrm{cm^{-2} \ s^{-1}})$

$F(>\Phi)$

Figure 18